

26 to a cellulose ribbon that can reach several microns in length and combine with ribbons from
27 other cells to form a robust biofilm matrix. We were able to take direct measurements in a near-
28 native state of the cellulose sheets. Our results also reveal a novel cytoskeletal structure, that
29 we name the cortical belt, adjacent to the inner membrane and underlying the sites where
30 cellulose is seen emerging from the cell. We find that this structure is not present in other
31 cellulose-synthesizing bacterial species, *Agrobacterium tumefaciens* and *Escherichia coli* 1094,
32 which do not produce organized cellulose ribbons. We therefore propose that the cortical belt
33 holds the cellulose synthase complexes in a line, to form higher-order cellulose structures such
34 as sheets and ribbons.

35

36 **Importance**

37 This work's relevance for the microbiology community is two-fold: It delivers for the first time
38 high-resolution near-native snapshots of the *Gluconacetobacter* spp. (previously
39 *Komagataibacter* spp.) in the process of cellulose ribbon synthesis, in their native biofilm
40 environment. It puts forward a non-characterized cytoskeleton element associated with the side
41 of the cell where the cellulose synthesis occurs. This represents a step forward in the
42 understanding of the cell-guided process of crystalline cellulose synthesis, particularly studied
43 in the *Gluconacetobacter* genus and still not fully understood. Additionally, our successful
44 attempt to cryo-FIB mill through biofilms to image the cells in their native environment will
45 drive the community to use this tool for the morphological characterization of other studied
46 biofilms.

47

48 **Introduction**

49 Humans rely on cellulose for building material, clothing and fuel¹⁻³. More recently the polymer
50 has sparked interest in the biotechnology field as a potential source of biofuel feedstock⁴, and

51 in the biomedical industry as a biologically neutral scaffold to promote tissue regeneration^{5,6}.
52 Cellulose is a linear polymer of glucose molecules connected with β 1-4 linkages by a
53 glucosyltransferase. Individual linear glucan chains can pack via hydrogen bonding and Van
54 Der Waals interactions in various ways to form different types of celluloses, with different
55 properties^{3,7,8}. The most common way glucan chains organize in nature is to form hydrogen-
56 bonded planes stacked into parallel layers via Van Der Waals interactions^{9,10}. These stacked
57 layers give rise to cellulose I microfibrils, or “native cellulose”, that can then coalesce to form
58 larger arrays. Because glucan chains pack in a regular lattice but cannot sustain this regular
59 pattern over their entire length, cellulose I is considered paracrystalline. Depending on how the
60 lattice is organized, cellulose I can be of the α form, bearing a triclinic unit cell, or β form,
61 bearing a monoclinic unit cell^{11,12}. Cellulose I β is mainly found in plants, where it is a major
62 structural element of the cell wall¹³.

63
64 In the prokaryotic world, cellulose is an important component of bacterial biofilms^{14,15}, which
65 increase cells' tolerance for a range of biotic and abiotic stresses and enhance surface adhesion,
66 cell cooperation and resource capture¹⁴. Cellulose-containing biofilms have also been involved
67 in pathogenicity, enabling bacteria to resist antibiotics and disinfection^{16,17}. Most cellulose-
68 synthesizing bacteria produce amorphous (non-crystalline) cellulose, but a few genera,
69 including *Gluconacetobacter*, can produce cellulose I α microfibrils. In *Gluconacetobacter*,
70 these paracrystalline cellulose microfibrils can further aggregate into wide ribbon structures
71 and larger arrays¹⁸, giving rise to thick biofilms that are predominantly pure cellulose I.

72 Bacterial cellulose is synthesized by an envelope-spanning machinery called the Bacterial
73 Cellulose Synthase (BCS) complex, encoded by the BCS gene cluster and first identified in
74 *Gluconacetobacter*¹⁵. While the components vary, most of the species encode BcsA, a
75 component in the inner membrane that, with BcsB, catalyzes transfer of UDP-glucose to the

76 nascent glucan chain^{15,19,20}. BcsD forms a periplasmic ring thought to gather glucan chains from
77 several BcsA/B units^{21,22}. BcsA and B are essential for cellulose synthesis *in vivo*, and BcsD is
78 essential for the crystallization of nascent glucan chains²³. BcsC forms a pore in the OM and
79 very recent work has solved its crystallographic structure²⁴. Consistent with previous data
80 relying on sequence homology with the exopolysaccharide secretin components AlgE and AlgK
81 from *P. aeruginosa*, BcsC is found to form an outer-membrane β -barrel pore at its C-terminal
82 end, secreting the nascent elementary cellulose fibrils into the environment^{23–27}. It is
83 hypothesized that the elementary cellulose fibrils can aggregate with neighboring elementary
84 fibrils upon secretion to form microfibrils^{28,29}. Genes flanking the operon, *cmcAx* (endo- β -1,4-
85 glucanase), *ccpAx* (unknown function) and *bglxA* (β -glucosidase), are essential for cellulose
86 crystallization and despite knowledge of their enzymatic functions, how they take part in this
87 process is unclear^{29–32}.

88 In the following report, the terms used to describe the cellulose assembly process are adapted
89 from the ones defined in²⁹, elaborating on the cell-directed hierarchical model for cellulose
90 crystallization^{7,10}. Glucan chains are linear polymers of β -1,4 linked glucose residues
91 synthesized by a single catalytic site of a cellulose synthase. An elementary fibril (also termed
92 mini-crystal in previous work^{10,33,34}) is the product of the periplasmic aggregation of multiple
93 glucan chains which is then extruded through a single BcsC subunit into the environment.
94 Microfibrils result from the aggregation of several elementary fibrils, at least three according
95 to earlier work³⁴, outside the cell. These microfibrils can then crystallize into sheets that stack
96 on each other to form ribbons. The latter terminology differs somewhat with previous usage in
97 that our definition of a sheet is equivalent to the “bundles of microfibrils”, the polymerization
98 step prior to the ribbon, described in²⁹.

99 Much work has already been done to understand the synthesis of paracrystalline
100 cellulose^{18,20,21,23,30–33,35–41}. In particular freeze-fracture/freeze etching electron microscopy

101 (EM) studies have found that the *G. hansenii* BCS complexes are arrayed linearly along the
102 side of the cell^{18,33,38,39}, and this arrangement seems to determine the extracellular organization
103 of cellulose I into ribbons^{18,33,39}. How this linear arrangement is achieved is not known.

104

105 Here we used cryo-electron tomography (cryo-ET) of isolated cells and cryo-Focused Ion Beam
106 (FIB)-milled biofilms to visualize native cellulose production in *G. hansenii* and *G. xylinus*,
107 allowing the morphological characterization of the cellulose ribbons in a near-native state. We
108 identified a novel cytoplasmic structure, which we call the cortical belt. We found that this
109 cortical belt is absent from *Escherichia coli* 1094, which produces amorphous cellulose, and
110 *Agrobacterium tumefaciens*, which produces crystalline microfibrils but not higher-order
111 sheets, suggesting that the cortical belt functions to align BCS complexes to produce cellulose
112 sheets.

113

114 **Results**

115 Cellulose is laid out in stacked sheets on one side of the cells.

116 To visualize bacterial cellulose production, we used cryo-ET to image intact frozen-hydrated
117 *G. hansenii* cells separated from their cellulose biofilm according to the original method from
118 Brown et al. 1976. Previous work showed that newly synthesized cellulose ribbons are visible
119 under the electron microscope at one hour post-separation³⁸. To assure that the cells would have
120 enough time to synthesize cellulose ribbons we imaged cells 5 hours (300 minutes) after
121 separation. To confirm cellulose production, we stained cells with mitoTracker Deep Red FM
122 to visualize membranes and Calcofluor-White to visualize cellulose. By confocal imaging, we
123 observed cellulose filamentous structures tens of microns long (Fig. 1A and B, cyan
124 arrowheads). We next plunge-froze cells at the same timepoint and imaged them by cryo-ET.
125 The rod-shaped cells always lay flat on the grids, but their long axis was oriented randomly in

126 the grid plane. Of 33 cells imaged, we found putative cellulose ribbons associated with 29
127 (88%), always on one side of the cell, including the top and bottom, and always aligned with
128 the cell's long axis (Fig 1C-E, yellow arrows). To confirm that the ribbon was in fact cellulose,
129 we treated cells with cellulase and observed a large reduction in the occurrence of ribbons in
130 cryo-EM and negative stained images (Supplemental figure 1, yellow arrowheads). Instead, we
131 observed aggregated material we think is likely partially digested cellulose (Supplemental
132 figure 1F, orange arrowheads).

133 The spatial relation between the cellulose ribbons and the OM was examined. In 3 out of the
134 29 tomograms, the cellulose ribbon was observed running beneath or on top of the cell, causing
135 it to be normal to the electron beam thus inherently not well resolved and difficult to assess its
136 spatial relation with the OM⁴². Therefore, data from these 3 tomograms was excluded for these
137 measurements. In the remaining tomograms two distinct configurations were observed: a
138 “tight” configuration in 23 out of 26 tomograms (88%), where the average outer membrane
139 (OM)-to-ribbon distance was 16 ± 5 nm ($n = 23$) (Fig. 1C-H, supplemental video 1,
140 <https://figshare.com/s/74891ac625fe8125c60c>), and a “loose” configuration in 3 out of 26
141 tomograms (12%), where the average OM-to-closest sheet distance was 99 ± 49 nm ($n = 3$)
142 (Fig. 2), most probably resulting from a mechanical stress resulting in the cellulose ribbon to
143 pull away from the cell. Among the tomograms showing a “tight” configuration, 17 out of 23
144 (65%) displayed multiple clear direct contacts between the OM and the ribbon (Fig. 1F-H, white
145 arrows). Tomograms in the “loose” configuration exhibited ribbons that seemed detached from
146 the OM, with an increased OM-to-closest sheet distance compared to the “tight” configuration
147 (Fig. 2E). All three tomograms presented disorganized aggregates bearing a mesh-like
148 appearance between the OM and the ribbon (Fig. 2A-D, orange asterisks and dashed bracket).
149 These aggregates always connected to the ribbon (Fig. 2A, black lined orange arrows).
150 Throughout the study and in line with previous studies, *G. hansenii* was never seen harboring

151 a flagellum, pilli, curli or any other appendages other than the cellulose ribbons (Supplemental
152 figure 2). Additionally, similar cellulose aggregates have been seen previously by negative
153 staining^{18,28}, hence we are confident that these structures are cellulose in a disorganized form.
154 These cells and their cellulose structures (the ribbons) were imaged in a near-native (frozen
155 hydrated) state, allowing measurement of their native dimensions. In our description of the
156 cellulose ribbons below, by length we mean the dimension parallel to the long axis of the cell
157 (Fig. 3A). By thickness we refer to the dimension normal to the cell surface (Fig. 3A, black
158 inset). By width we refer to the dimension tangential to the cell surface (Fig. 3B). The cellulose
159 ribbons we observed were very similar to what has been seen previously by negative stain
160 EM^{28,38}. Ribbons comprised long flexible stacked sheets, too long to be measured by cryo-ET
161 because they are never entirely in the field of view. Relative to previous morphological work,
162 our flexible sheets equate to what was described as “microfibrillar bundles” in previous
163 studies^{10,28,29,34}. However, our observations in a frozen-hydrated state allowed us to visualize
164 them in a sheet-like configuration, therefore we chose to call them sheets instead of bundles.
165 Missing wedge-induced Z-elongation of the cellulose sheets distorts width measurements^{43,44}.
166 Despite this artefact, we estimated it at 38 ± 14 nm ($n = 45$) (Fig. 3C), which is therefore an
167 overestimate. To see if width increased along the cell, width estimates were performed along
168 the length of the cellulose ribbon in 3 tomograms. Unfortunately, these estimates are heavily
169 influenced by the missing wedge-induced elongation in the Z-dimension, therefore the
170 measurements did not give any conclusive trend in one way or another (increase, decrease or
171 constant width along the cellulose ribbon). These sheets then stack into a ribbon (2.3 ± 0.9
172 sheets on average; $n = 24$), with a variable inter-sheet distance (16 ± 7 nm; $n = 23$). Inter-sheet
173 distance was accurately measured peak-to-peak (Fig. 3D), which encompasses 2 halves of the
174 two neighboring sheets’ density and the space between them (Fig. 3A, black inset). Because
175 the apparent thickness of single densities in cryo-ET is strongly affected by the defocus applied,

176 individual cellulose sheet thickness measurements will be overestimated. Therefore, we can
177 only say confidently that they are thinner than the inter-sheet distance. Despite careful
178 inspection, although densities could be seen in the periplasmic space, we did not recognize a
179 consistent shape which we could confidently attribute to the BCS machinery. This is likely due
180 to the large cell diameter (~800nm), and the small size and/or flexibility of the BCS complexes.

181

182 Sheets arise from the stacking of microfibrils

183 To visualize earlier stages of cellulose synthesis, we plunge-froze cells at earlier timepoints
184 after separation from the biofilm. A total of 6 and 15 tomograms were acquired at 13- and 20-
185 minutes post-separation, respectively. At 13 minutes (the most quickly we could complete
186 plunge freezing), no cells exhibited a cellulose ribbon, however, disorganized aggregates were
187 observed in the vicinity of 1 out of the 6 tomograms. At 20 minutes post-separation, cellulose
188 ribbons were observed adjacent to the cell in 9 out of 15 tomograms (64% versus 88% (n = 33)
189 at 300 minutes post-separation) (Fig. 4A). Out of these 9 cells harboring an adjacent cellulose
190 ribbon, 3 had it on the top or bottom of the cell and were excluded from the analysis for the
191 same reason explained above. Therefore, the analysis of the OM-ribbon interface was
192 conducted on the remaining 6. The cellulose ribbons observed at 20min post-separation
193 comprised only one cellulose sheet (n = 6), significantly smaller amount than at 300min post-
194 separation (P-value <0.0001, Fig. 4B). Four out of these 6 tomograms (67%) exhibited a “tight”
195 configuration. The average OM-to-closest sheet distance of 14 ± 3 nm (n = 4) was not
196 significantly different from the 300 minutes post-separation “tight” configuration average OM-
197 to-closest sheet distance (P-value > 0.9, Fig. 4C-D, n = 4 and 23 for 20min and 300min post-
198 separation, respectively). The two other tomograms bore ribbons in the “loose” configuration,
199 i.e. at an OM-to-closest sheet distance >40 nm with disorganized aggregates in-between. These
200 “loose” ribbons had an OM-to-closest sheet distance of 43 and 59 nm, respectively. The

201 disorganized aggregates visible at 20 minutes post-separation emanated perpendicularly from
202 the OM to connect to the nascent cellulose sheet. They were thinner than the ones observed at
203 300 minutes post-separation and rod-shaped (Fig. 4E-F, red arrowheads). Average density
204 profiles normal to the direction of the cylindrical-shaped densities were traced to estimate their
205 diameter (Fig. 4G). We again emphasize the inherent overestimation of such measurements due
206 to defocus. The average estimates on the two cells, 11 ± 2 nm ($n = 12$) and 6.5 ± 1 nm ($n = 4$),
207 respectively (Fig. 4G), therefore establish upper limits of the true diameter. These estimates are
208 also less than the above-measured inter-sheet distances (Fig. 4H). Because elementary fibrils
209 are thought to be between 1.5 and 6 nm in thickness^{18,38,39}, we hypothesize these structures are
210 microfibrils composed of several elementary fibrils. The variability of the microfibril diameter
211 measurements between cells (Fig. 4G, Cells #1 and #2) suggests these structures can contain a
212 varying number of elementary fibrils more-or-less tightly packed together. This configuration
213 is reminiscent of what was seen in previous studies of microfibrils coming out of clusters of
214 pores^{28,38} and likely represents an early stage of cellulose sheet formation that has been
215 mechanically disturbed. Sheets at 20 minutes post-separation had an estimated width of 25 ± 8
216 nm ($n = 6$) (Fig. 4I), smaller than those at 300 minutes, although the difference did not appear
217 significant (P-value = 0.26).

218 These results show that 1) the microfibrils emanating from the OM have roughly the same
219 thickness as the cellulose sheet, 2) sheet width seems to increase over time and 3) the number
220 of cellulose sheets comprising a ribbon increases over time.

221

222 A novel cytoplasmic structure is associated with cellulose production

223 We next examined the interior of *G. hansenii* cells during cellulose synthesis. These cells had
224 extensive cytoplasmic vesicles in the center and at the periphery of the cell (Supplemental
225 figure 3), which is a rare and largely uncharacterized aspect of bacteria⁴⁵. The most notable

226 feature we observed was another ribbon-like structure closely associated with the inner
227 membrane (24 ± 4 nm from it; $n = 19$, for an example peak-to-peak measurement see Fig. 3D)
228 and several hundred nanometers in length (Fig. 5A, purple arrows). We found it in 90% of cells
229 with a cellulose ribbon ($n = 29$), always on the same side as, and underlying, the nascent
230 cellulose sheet (Fig. 5B-C, supplemental video 2
231 <https://figshare.com/s/74891ac625fe8125c60c>). This cytoplasmic structure is not a tube but
232 rather a stack of sheet-like structures, 47 ± 23 nm wide ($n = 10$), parallel to the inner membrane
233 and spaced (peak-to-peak) by 15 ± 5 nm ($n = 7$) (Fig. 5D-F). We refer to it here as the "cortical
234 belt". Interestingly, in tomograms acquired in shaking conditions in SH media supplemented
235 with cellulase, although the cellulose ribbons had vanished, the cortical belt was observed
236 (Supplemental figure 1F, purple arrows).

237

238 Structural hallmarks of crystalline cellulose synthesis are also present in intact biofilms

239 It is possible that separating bacteria from the cellulose mat for whole cell cryo-ET imaging
240 could have altered structures associated with cellulose synthesis. We therefore imaged *G.*
241 *hansenii* cells *in situ* in young cellulose biofilms grown on gold grids. We imaged biofilms after
242 3 or 6 hours before plunge-freezing in hope of visualizing any change in the ordering of the
243 fibers or the aspect of the cells over the course of biofilm growth. To access cells within the 5-
244 to 10-micron thick biofilm, we used cryo-FIB milling to generate thin (~200 nm) lamellae
245 suitable for imaging by cryo-ET (Fig. 6A-C). In a total of 19 analyzed tomograms (9 and 10
246 tomograms for 6h and 3h biofilms, respectively, Table 1), we observed fields of living and dead
247 bacteria encased in a matrix of bundled cellulose ribbons at both time points (Fig. 6D-E and
248 supplemental video 3 <https://figshare.com/s/74891ac625fe8125c60c>). Overview tomograms
249 (low magnification with low total dose) and high-resolution composite images of the lamellae
250 allowed extraction of positional information of the cells in relation to the biofilm. There were

251 0.10 ± 0.02 and 0.27 ± 0.04 cells/ μm^2 and 15% and 28% of the volume of the lamellae was
252 occupied by cells at 3 and 6h time points, respectively (Fig. 6F) ($n = 6$ and 4 lamellae,
253 respectively). This approximate 2-fold increase in cell density from a 3-hour to a 6-hour biofilm
254 suggests that cell division is occurring during biofilm growth.

255 Dead cells can be easily differentiated from living cells (Fig. 6D, red asterisks) by the wavy
256 aspect of their envelope, sometimes presenting punctures and by the appearance of their cytosol.
257 Living cells typically have ribosome-rich and nonribosomal regions (bacterial chromosome)
258 while dead cells have coagulated cytosols with large electron-dense aggregates and very low
259 ribosome counts. The live-to-dead cell ratio was calculated at 0.9 ± 0.1 in both 3- and 6-hour
260 biofilms, revealing no increase in the proportion of dead cells between these two timepoints
261 (Fig. 6G). Because lamellae give access to the native organization and layering of the cells
262 within the biofilm, the depth of dead/living cells within the biofilm was assessed by measuring
263 their distance from the leading edge of the lamella (see methods). No trend between cell depth
264 within the biofilm and state of the cells was detected (Fig. 6H).

265 In all 19 tomograms (combining 3h and 6h lamellae), we observed numerous cellulose ribbons
266 surrounding the cells (Fig. 7A, yellow arrowheads). In 5 out of the 19 tomograms (26%), a
267 cellulose ribbon was closely appended to the cell's OM, as we previously had seen in separated
268 cells (Fig. 7B-C, dark-lined yellow arrowhead). Among those 5 tomograms, 4 showed a cortical
269 belt adjacent to the cellulose ribbon (Fig. 7B-D and supplemental video 3
270 <https://figshare.com/s/74891ac625fe8125c60c>). The OM-to-cellulose ribbon distance ($19.2 \pm$
271 8 nm, $n = 4$) and inner membrane to cortical belt distance (22 ± 2 nm, $n = 4$) were very similar
272 to those measured before in separated cells. In 5 out of the 10 tomograms in 3h biofilm lamellae,
273 disorganized cellulose aggregates were observed connected to well-ordered ribbons just as in
274 the separated cells, whereas this was never observed in the 6h biofilms. This suggests that
275 crystallization is disrupted more often in early biofilm growth (Fig. 7E-G, orange dashed

276 lining). Because *Gluconacetobacter* cells are thick, electron transmittance in the central region
277 of the cytoplasm is very low when imaging whole cells, making it difficult to visualize this
278 area. Reducing sample thickness to approximately 200 nm by cryo-FIB-milling allowed us to
279 observe these central regions with greater contrast and visualize the extensive vesicle network
280 deep inside the cell (Fig. 7E, white arrowheads) while losing the ability to capture the full extent
281 of the cellulose sheet stacking because of the lamellar sampling.

282

283 The cortical belt is specific to bacterial species that produce crystalline cellulose ribbons

284 To see whether the cortical belt is specific to *G. hansenii*, we imaged another species of
285 *Gluconacetobacter*, *G. xylinus* (also referred to as *Komagataibacter sucrofermentans* BPR-
286 2001), by cryo-ET at 300 minutes post-separation. *G. xylinus* is a species isolated from cherry,
287 originally called *Acetobacter xylinum* bearing the ability to produce an increased amount of
288 cellulose in shaking culture conditions³⁵. *G. hansenii* and *xylinus* have diverged quite
289 substantially and differ in their GC content, and *G. hansenii* has its *bcsA* and *bcsB* genes fused
290 and harbors no gene clusters associated with acetan metabolism, commonly found in other
291 *Gluconacetobacter* species⁴⁶. In our hands, we also observed that *G. xylinus* biofilms seem to
292 grow more slowly and are stiffer in comparison to *G. hansenii* biofilms. Four out of 8 cells
293 (50%) exhibited an extracellular cellulose ribbon along the cells' long axis (Supplemental
294 figure 4A). The cellulose ribbons observed had 2 sheets of cellulose, with an estimated average
295 width of 27 ± 16 nm ($n = 5$). All four cells also possessed a cortical belt (Supplemental figure
296 4A-B, purple arrows), with similar dimensions to those in *G. hansenii*. The average distance
297 from the cortical belt to the inner membrane was 24 ± 4 nm ($n = 4$). In one instance, the cortical
298 belt also contained three stacked layers spaced (peak-to-peak) by 9 nm (Supplemental figure
299 4C). Aside from *Gluconacetobacter*, other bacterial species produce different types of
300 cellulose. For instance, *Escherichia coli* 1094 can make amorphous cellulose⁴⁷ and

301 *Agrobacterium tumefaciens* makes paracrystalline cellulose microfibrils during plant
302 infection⁴⁸. Neither of these species are known to make cellulose ribbons, though. We asked
303 whether structures similar to the cortical belt observed in *Gluconacetobacter* were present in
304 these species. Our lab had previously imaged *A. tumefaciens* for other studies, and therefore
305 cryo-tomograms of *A. tumefaciens* were already available. We confirmed by confocal
306 microscopy that *A. tumefaciens* produces cellulose in the same growth conditions as had been
307 used for the earlier experiments (Fig. 8A), and then screened the available tomograms for the
308 presence of cellulose. As the purpose of the previous studies had not been cellulose synthesis
309 observation, relatively few (65 out of 1,854 tomograms) showed distinct cellulose fibers in the
310 vicinity of the cells (Fig. 8B-C, yellow arrowheads, supplemental video 4
311 <https://figshare.com/s/74891ac625fe8125c60c>). These fibers did not adopt any preferential
312 orientation and ran in all directions around the cell. They also had a decreased width (14 ± 5
313 nm, $n = 52$ fibers measured in 5 tomograms) compared to *G. hansenii* cellulose sheets (P-value
314 <0.0001), confirming that *A. tumefaciens* does not elaborate wide cellulose sheets nor ribbons
315 but rather simpler structures of crystalline cellulose, presumably bundles of microfibrils. In the
316 65 cellulose-producing cells, we never observed a cortical belt structure. Two notable features
317 were however observed: 1) a polar outer-membrane flattening in 28 cells with a thickening of
318 the OM (43% out of the 65 cells presenting cellulose, Fig. 8B, cyan arrow) and 2) polar
319 amorphous aggregates in 24 cells (37% out of the 65 cells presenting cellulose), (Fig. 8B,
320 orange dashed lining). 19 cells exhibited all three described features, the polar flattening, the
321 amorphous aggregates and the cellulose fibers. We suspect these polar amorphous aggregates
322 to be the unipolar polysaccharides (UPP) described in previous work and shown to allow the
323 attachment of *A. tumefaciens* to biotic and abiotic surfaces in the early stages of biofilm
324 formation⁴⁹. The very close proximity of the putative UPP to the polar flattening suggests the
325 latter could hold the UPP-secreting complexes.

326

327 We confirmed that *Escherichia coli* 1094 grown in minimal medium produces cellulose (Fig.
328 8D). The cells aggregated, making it difficult to image single cells by cryo-ET, so instead we
329 FIB milled through bacterial mats, producing approximately 200 nm-thick lamellae. To identify
330 cellulose structures, we also imaged lamellae from cultures grown in minimal medium
331 supplemented with cellulase. In 3 of the 5 tomograms of untreated cells, we observed
332 amorphous fibrous material (Fig. 8E, orange asterisk), that was not visible in 2 tomograms of a
333 cellulase-treated culture (Fig. 8F). None of the cells imaged in either condition contained a
334 cortical belt (n = 13 untreated and 5 cellulase-treated cells), suggesting that it is unique to
335 bacteria producing higher-order paracrystalline cellulose structures, *i.e.* sheets.

336

337 **Discussion**

338 Here we characterized bacterial cellulose synthesis in two *Gluconacetobacter* species and
339 compared it to two other species by cryo-ET. We identified a novel cytoplasmic structure
340 associated with the production of cellulose I ribbons in *Gluconacetobacter* spp. We also
341 performed cryo-FIB milling followed by cryo-ET on native biofilms.

342

343 Cryo-ET confirms the need of a tight interaction between the nascent sheet and the OM

344 The cell-directed hierarchical model proposes linearly arranged 3.5-nm diameter pores on the
345 surface of the cell³⁹, each extruding an elementary fibril^{28,33}. The arrangement of these pores in
346 lines allows the crystallization of the elementary fibrils upon secretion and integration into a
347 cellulose sheet parallel to the long axis of the cell^{7,50,51}. Our results agree with this model.
348 Indeed, we observed that when the gap between the nascent sheet and the OM exceeds
349 approximately 40 nm, disorganized aggregates occur (Fig. 2). Along with previous work that
350 observed similar events²⁸, we hypothesize that these aggregates are microfibrils failing to

351 integrate into an ordered sheet. Furthermore, it has been shown that the addition of compounds
352 which bind directly to cellulose drastically alters the assembly of the sheets and leads to the
353 formation of similar aggregates^{18,28,51}. It appears as though preventing the nascent microfibrils
354 from interacting with each other upon secretion prevents them from forming one organized
355 sheet. Conversely, a confined spacing between the nascent sheet and the OM promotes proper
356 crystallization of the nascent microfibrils. This proximity could be maintained either by a
357 previously synthesized sheet preventing the nascent one from separating too far from the OM,
358 or by specialized cellulose binding enzymes situated in the outer-leaflet of the OM, such as
359 CmcAx, which has the ability to bind cellulose⁵².

360

361 Cryo-ET sheds light on the buildup of a microfibril

362 Many values have been reported for the elementary fibrils' dimension, mainly through direct
363 observation by negative staining electron microscopy^{18,33,38}. The most favored hypothesis is an
364 approximately 1.5-nm thick elementary fibril (thoroughly discussed in²⁸). Very recently, the
365 characterization of the structure of the BcsC subunit (the OM pore) describes a 1.5 nm inner-
366 diameter pore with a very narrow constriction caused by a mobile gating loop, restricting the
367 channel to a 0.2 nm bottleneck²⁴. It is however not known to what extent this gating loop can
368 open the pore. Therefore, two hypotheses arise: 1) one BcsC pore can accommodate a 1.5 nm
369 elementary fibril through an opening of the gating loop or 2) it can accommodate a smaller
370 elementary fibril, perhaps only a single glucan chain. In the latter case the building of the
371 elementary fibril would then take place upon secretion of the glucan chains in the environment.
372 While negative staining has provided high-resolution views of cellulose ribbons^{28,38}, observing
373 them in a frozen-hydrated state enables more accurate measurements of their dimensions and
374 observation of their interaction with the OM. This is particularly important for extracellular

375 polysaccharides, which have been shown to collapse and undergo drastic conformational
376 changes upon dehydration, staining and embedding⁵³.

377 We were able to image in two tomograms, microfibrils extruded perpendicularly to the OM and
378 integrating to form a thin parallel sheet (Fig. 4E-F). A possible interpretation of why these
379 events are rare is that they result from an accidental mechanical separation of the nascent sheet
380 from the OM, revealing early forms of cellulose bundling such as thin microfibrils. As
381 explained earlier, precise measurement of the thickness of densities is difficult in cryo-ET since
382 it is influenced by the defocus applied during imaging (causing overestimation of the true
383 thickness). Despite this uncertainty, our measurements are done in a near native state. We
384 estimated these microfibrils to be less than 11 nm in diameter (Fig. 4G-H), in line with previous
385 work which measured microfibril thicknesses from 3 to 12 nm in cellulose sheets splayed apart
386 by cellulase treatments⁵⁴. If we assume an elementary fibril is 1.5 nm in diameter and that it
387 can go through a single BcsC subunit, an 11 nm diameter cylindrical microfibril (maximal
388 thickness estimation) would comprise 53 elementary fibrils. This would require a cluster of 53
389 BcsC subunits. Previous reports have stated the cellulose extrusion pores cluster in linear
390 bunches of 2 to 4 pores^{7,33}. Accommodating both observations would require that there is more
391 than one BcsC subunit per extrusion pore. For example, if each 3.5 nm diameter extrusion
392 pore³⁹ maximally held 5 BcsC subunits, a cluster of 11 extrusion pores could produce an 11
393 nm diameter microfibril (Fig. 9). In this case, each extrusion pore holding multiple BcsC
394 subunits would produce a crystalline aggregate of elementary fibrils which would pack with its
395 neighboring aggregates to form a microfibril.

396

397 Cryo-ET sheds light on the assembly of a cellulose sheet

398 We found that ribbons were stacks of sheets that likely interact loosely with one another since
399 the inter-sheet distance varied from 7- to 31-nm. This loose stacking corroborates previous

400 observations³⁴. Previous measurements done by negative staining had estimated cellulose sheet
401 width to range from 40 to 600 nm^{28,38,54}, wider than our measurements ranging from 11 to 69
402 nm (Fig. 4I). These variations have been attributed to the cell strain, growth conditions and
403 intercellular variation^{28,38,39}. We found that the thickness of cellulose sheets is similar to the
404 diameter of the microfibrils. Therefore, our data suggest that microfibrils lie down in rows to
405 create the width of the sheet. This was also suggested in⁷.

406

407 While the number of sheets produced by a single cell increased with time, the main dimension
408 of growth appears to be ribbon length, as suggested by previous work and our fluorescence data
409 showing cellulose ribbons several cell lengths long (Fig. 1A-B)²⁹. Wider sheets occur in later
410 time points (Fig. 4I), suggesting that sheet width also grows with time. However, in the current
411 model, sheet width is correlated with the number of extrusion pores, hence to cell length^{7,39}. It
412 is possible that at 300min post-separation, cells are longer and possess more extrusion pores,
413 therefore producing wider sheets. As mentioned earlier, our attempt to observe this by
414 monitoring sheet width along its length failed. The magnification employed to acquire the data
415 would only allow us to capture partial lengths of the cells and their cellulose ribbon. We think
416 that upon the segments we captured, the sheet width increase or decrease, probably in the range
417 of 10 to 20 nm, was unlikely to be observe because of the estimates being heavily influenced
418 by the missing wedge.

419

420 Cryo-ET on *G. hansenii* cells allowed the visualization of a novel cytoskeletal element, the
421 cortical belt

422 Negative stain, cryo-fracture and immuno-EM studies have shown that cellulose extrusion
423 pores in *Gluconacetobacter* align in a line on one side of the cell^{28,39,55}, but what causes this
424 alignment is unknown. Here, we identify a novel cytoplasmic structure in two species of

425 *Gluconacetobacter* that spatially correlates with the nascent cellulose ribbon (Fig. 1C-E and
426 Fig. 5). This structure, which we term the cortical belt, is found at a fixed distance from the
427 inner membrane (24 ± 4 nm) and remains intact upon cellulase treatment in shaking conditions
428 (Supplemental figure 1F, purple arrow), suggesting that it is stable even in the absence of the
429 cellulose ribbon and in turbulent culture conditions.

430 We observed the cortical belt in both *Gluconacetobacter* spp. imaged but not in other bacteria
431 that produce less-ordered forms of cellulose, including *Escherichia coli* 1094, which
432 synthesizes amorphous cellulose⁴⁷, and *Agrobacterium tumefaciens*, which synthesizes
433 cellulose I microfibrils⁵⁶ (Fig. 8). This suggests the cortical belt is a peculiar cytoskeletal
434 filament only found in the *Gluconacetobacter* genus. Its striking spatial colocalization with the
435 extracellular cellulose ribbons leads us to propose that the cortical belt functions in the
436 formation of cellulose ribbons. The periplasmic BcsD and its interacting partner CcpAx^{22,31}, as
437 well as two cell wall-related enzymes, have been shown to be involved in the crystallization
438 process of the ribbons^{29,31,57}. It is possible that the cortical belt interacts with one or more of
439 these components to guide the positioning of the BCS complexes. Unfortunately, as stated
440 earlier, we failed to identify any repeated density above the cortical sheet that could be
441 associated to the secreting complexes. However, the thick cells and crowded periplasm
442 obscured and very likely masked relevant densities. Moreover, it is unknown whether these
443 secreting complexes are channels spanning the periplasmic space, given the structures of the
444 individual components^{19–21,24,58}. Their predicted position in the membranes shows very small
445 portions protruding in the periplasm. We therefore think the BCS complexes are too
446 small/flexible for particle picking and sub-tomogram averaging in such a crowded environment.
447 If the cortical belt is responsible for scaffolding the BCS complexes, it represents a novel
448 prokaryotic cytoskeletal element, i.e. “a cytoplasmic protein filament and its associated
449 superstructures that move or scaffold material within the cell”⁵⁹. Other bacterial cytoskeletal

450 elements have been observed to form belt-like structures, including bactofilins⁶⁰, or to stack,
451 like the CTP synthase⁶¹, although with different dimensions. We hope that future work will
452 identify the component(s) that form the cortical belt, shedding more light on the molecular
453 processes involved in the organization and clustering of the BCS complexes in *G. hansenii*.

454

455 The cortical belt reveals another similarity between cellulose synthesis in *Gluconacetobacter*
456 and land plants.

457 Historically, the first plant cellulose synthase genes were identified by cDNA homology with
458 the *G. xylinum* acsA (bcsA) gene⁶². Later on, phylogenetic studies highlighted an early
459 divergence between cyanobacterial and plant cellulose synthases^{63,64}. A large number of
460 cellulose I synthesizing organisms have in common that the synthase complexes arrange in
461 specific patterns, determining the final architecture of the cellulose structures⁷. A simple row
462 in systems like *Gluconacetobacter* spp. or certain charophytes and chlorophytes⁶⁵ and
463 hexameric rosette structures called Cellulose Synthase Complexes (CSC) in land plants. In
464 both, the extrusion of a crystalline form of cellulose exerts a force believed to be able to propel
465 the CSCs in plants^{66,67} and the whole cell in *Gluconacetobacter*^{29,38}. Our work uncovers an
466 additional similarity, the involvement of a cytoskeletal element, the cortical belt, to guide the
467 synthase complexes. In land plants CSCs have been shown to interact indirectly with underlying
468 cortical microtubules, mediating trans-membrane cross-talk⁶⁸⁻⁷⁰, guiding and regulating CSC
469 velocity⁷¹⁻⁷³. While CSCs were shown to be motile in land plants, they are believed to be static
470 in *Gluconacetobacter*²⁸, perhaps held in place by the cortical belt, in order to transfer the
471 propelling force to the whole cell.

472

473 Insights from FIB-milling native biofilms

474 Cryo-FIB milling through native biofilms offers the possibility of observing bacteria in the
475 context of their original biofilm environment and retrieving high resolution morphological and
476 positional information about the cells relative to one another and relative to the biofilm layers.
477 Visualization of the density and organization of the extracellular matrix and its interaction with
478 the cells is also rendered possible by cryo-FIB milling. This is especially important since in
479 nature most bacterial species are found in complex interacting communities, in the form of
480 homogeneous or heterogeneous communities that organize in biofilms¹⁴.

481 Milling the *Gluconacetobacter* biofilms to 200 nm revealed numerous cytosolic vesicles of
482 variable shapes and sizes. Although we were not able to connect the presence of these numerous
483 vesicles with the process of cellulose production, cytosolic vesicles in bacteria are uncommon
484 but have already been observed several times in *M. xanthus*, *A. tumefaciens* and *E. coli* for
485 example⁴⁵. Their detailed structure, function and biogenesis are not known. The cortical belt
486 was also visible, as in the isolated cells. The cellulose ribbons aligned with each other to form
487 larger arrays 2-3 μm wide (Fig. 6D, yellow arrowheads and supplemental video 3
488 <https://figshare.com/s/74891ac625fe8125c60c>), showing the propensity of these structures to
489 interact with each other. This propensity was previously characterized by live imaging of the
490 cellulose biosynthesis and crystallization process in *Gluconacetobacter*, which showed that the
491 bacterial cells preferentially follow already established tracks, *i.e.* previously synthesized
492 cellulose ribbons²⁹. The occurrence of disorganized cellulose clusters in biofilms grown for 3h
493 but not 6h, suggests that such aggregates are either 1) digested by enzymes, likely CmcAx,
494 reported to have an endoglucanase capable of digesting amorphous cellulose⁷⁴ and to be present
495 on the surface of *G. hansenii* or released in the environment^{30,52} or 2) diluted by a gradual
496 increase in well-ordered ribbons over time.

497 Cell death in biofilms, with the fraction of dead cells measured at 10% in our biofilms, is a
498 well-known phenomenon¹⁴, caused by programmed cell death mechanisms, cannibalistic

499 behaviors such as already described in *B. subtilis*⁷⁵ or nutrient/oxygen depletion^{76,77}. We did
500 not observe a preferential location of dead cells at the bottom of the biofilm, ruling out anoxic
501 conditions being the primary cause of cell death. This could be because the thickness of the
502 biofilm, between 1.5- and 3- μm according to the cell depth distribution (Fig. 6H), is too small
503 to have a significant oxygen gradient, as suggested by studies that measured total anoxia being
504 reached generally between 70- and 80- μm depth⁷⁷⁻⁷⁹. Processing thicker biofilms in the range
505 of tens of microns would allow visualization of the effects of nutrient/oxygen gradients on cell
506 distribution and physiology. For now, plunge freezing such as performed in this study can only
507 properly vitrify samples less than ~ 10 microns thick⁸⁰. Moreover, milling thicknesses above 8-
508 10 microns becomes labor intensive and technically difficult. A possible course of action for
509 further studies would be to perform high-pressure freezing on thicker biofilms and then produce
510 thin sections either by cryosectioning, hybrid cryosectioning/FIB-milling methods such as
511 described in⁸¹⁻⁸³ or following a cryo-lift out procedure⁸³.

512

513

514 **Conflicts of interest**

515 The authors declare that there are no conflicts of interest.

516

517 **Acknowledgments**

518 This work was supported by NIH grant R35-GM122588 to GJJ, the Howard Hughes Medical
519 Institute (HHMI) and the Center for Environmental Microbial Interactions (CEMI) pilot grant
520 program. Cryo-electron microscopy was performed in the Beckman Institute Resource Center
521 for Transmission Electron Microscopy at Caltech. We thank Jean Marc Ghigo for kindly
522 providing us the *E. Coli* 1094 strain. Special acknowledgments to Catherine Oikonomou for all

523 the help and scientific advice given during this study and also to Candace Haigler for sharing
524 her thoughts and her precious experience on the not so common *Gluconacetobacter* spp.

525

526 **Methods**

527 Cell culture

528 *Gluconacetobacter hansenii* (ATCC 23769) was cultured as previously described³⁷ in SH
529 medium: 2% glucose, 0.5% bactopectone, 0.5% yeast extract, pH 6. For solid medium, 2.5%
530 bacto-agar was added. Cells were separated from the cellulose biofilm by mechanical disruption
531 as previously described³⁸. Briefly, the bacterial cellulose biofilm developing at the air-media
532 interface was picked up with a single-use sterile inoculating loop and transferred to fresh
533 medium, where it was vigorously shaken and then removed. In preparation for freezing, cells
534 were pelleted by centrifugation for 10 minutes at 2500rcf at 20C and resuspended in 0.5mL of
535 SH media. The culture was incubated for the desired length of time at 30°C without shaking
536 before plunge freezing. For cellulose digestion, 0.2g/L cellulase (Worthington, purified exo-
537 and endo-glucanases, #LS002598) was added.

538

539 *Gluconacetobacter xylinus* (ATCC 700178/BPR2001) was cultured as described above in
540 Fructose–Peptone–Yeast Extract (FPY) media: 2% fructose, 1% bactopectone, 0.5% yeast
541 extract and 0.25% K₂HPO₄.

542

543 *Escherichia coli* 1094 was cultured in Lysogeny Broth (LB) and induced for cellulose
544 production in minimal medium: 0.2% (NH₄)₂SO₄, 1.4% KH₂PO₄, 0.1% MgSO₄, 0.5%
545 FeSO₄·7H₂O, 0.4% glucose, 0.01% thiamine, pH 7. A saturated overnight LB culture was
546 diluted 1:50 into 3mL of minimal medium with or without 0.2g/L cellulase (Worthington,
547 purified exo- and endo-glucanases, #LS002598). Cultures were incubated at 37°C with shaking

548 at 220rpm. When the medium transitioned from turbid to clear and white flakes appeared
549 (cellulose and bacteria), the induction of cellulose synthesis is considered successful.

550

551 *Agrobacterium tumefaciens* was cultured as described in previous work⁸⁴. Briefly, *A.*
552 *tumefaciens* C58 was cultivated in liquid AB medium (glucose 0.2%, NH₄Cl 18.7mM, MgSO₄
553 2.5uM, KCl 2mM, CaCl₂ 0.07mM, FeSO₄ 0.01mM, K₂HPO₄ 8.4mM, NaH₂PO₄·7H₂O
554 4.16mM, pH 7) at 30C overnight. Induction was done by pipetting 100uL of overnight culture
555 and spreading onto AB induction plates (glucose 0.2%, NH₄Cl 18.7mM, MgSO₄ 2.5uM, KCl
556 2mM, CaCl₂ 0.07mM, FeSO₄ 0.01mM, K₂HPO₄ 8.4mM, NaH₂PO₄·7H₂O 4.16mM, Bactagar
557 1.7%, Acetosyringone 100uM, pH 5.8). Plates were then incubated for 3 days at 20C. Cells
558 were resolubilized by scraping a small amount from the plate with an inoculation loop and
559 resuspending it in 100uL of liquid induction AB medium.

560 The following strains are the ones included in the tomogram analysis: **NT1** is a C58 strain
561 without the pTiC58 (tumor inducing) plasmid; **A139** strain is NT1REB(pJK270) + pJZ041.
562 NT1REB is a “bald strain”, no flagellin mutant, derived from NT1. The pJK270 is pTiC58 with
563 the transposed NPTII gene for kanamycin resistance. The pJZ041 plasmid carries a GFP tagged
564 VirB8 gene, a component of the T4SS (Aguilar et al. 2011); **JX148** strain is a C58 derived
565 mutant of the rem gene. The strain is non motile; **AD348** is a GV3101(pMP90) strain with its
566 whole VirB system deleted. GV3101 is a pTiC58 free, rifampicin resistant C58 strain and
567 pMP90 is a helper pTiC58 without the T-DNA; **AD1484** is a AD348 variant, transformed with
568 pAD2079 containing the whole VirB system.

569

570

571

572 Confocal microscopy

573 Cellulose was stained with Calcofluor-white (Sigma-Aldrich, #18909) at a concentration of
574 0.001% and cell membranes were stained with MitoTracker Deep Red FM (Thermo-Fisher,
575 #M22426) at a concentration of 0.5ug/uL. Stack acquisition was done on a Zeiss LSM880 Airy
576 Scan microscope. Airy scan acquisitions were performed in super-resolution mode with Z-step
577 set at the optimal optical sectioning. The Mito-Tracker Deep Red FM channel was set as the
578 following: excitation at 633 nm, use of the 488/561/633 main beam splitter and a band-pass
579 570-620 + long-pass 645 filter. The Calcofluor White channel was set as the following:
580 excitation at 405 nm, use of the 405 main beam splitter and a band-pass 420-480 + band-pass
581 495-550 filter. Airy scan processing was performed on the fly by the in-built algorithm of Zeiss
582 Black.

583

584 Sample preparation for cryo-EM

585 For isolated cells, Quantifoil Cu R2/2 Finder grids (*Quantifoil Micro Tools GmbH*) were glow-
586 discharged at 15mA for 1min. The grids were pre-incubated with fiducial marker solution
587 prepared as follows: 50μL of 10nm colloidal gold (*Ted Pella, Inc*) mixed with 50uL of 5%
588 BSA, vortexed 1 min and centrifuged at 15,000rcf for 15 min, supernatant discarded, and pellet
589 resuspended in 40μL of PBS buffer. 3μL were deposited on each grid, left for 1 minute then
590 back-blotted with Whatman paper. Cells were plunge frozen with a Vitrobot Mark IV (*Thermo*
591 *Fisher Scientific*) with 100% humidity at 30°C and back-blotted for 3 to 5s.

592

593 For native biofilms, Quantifoil gold R2/2 Finder grids were placed in 35mm glass bottom petri
594 dishes (*MatTek Corporation* #P35G-1.0-2.0C) containing 1mL of SH media inoculated with a
595 2-day old biofilm. The dishes were sealed with Micropore tape (*3M*) and incubated without
596 shaking at 30°C for 3 to 6 hours. Plunge-freezing was done at 22C, 50% humidity, either with
597 manual blotting on both sides of the grids (first back-blotted then front-blotted) or using the

598 automatic blotting function of the Vitrobot with a blot time of 5-6s, blot force of 15 and drain
599 time of 2s.

600

601 For *E. coli* 1094, after 4 hours of incubation in minimal media, the medium should turn from
602 turbid to clear with white flakes. OD₆₀₀ of the cultures was monitored using the culture (always
603 turbid) where cellulose induction was performed in the presence of cellulase to keep the cells
604 from aggregating. It was then used as a reference to concentrate the cells to high OD₆₀₀ (10-
605 20), in order to form bacterial mats on the EM grids, for control and cellulase conditions.
606 Plunge-frozen was done at 20C, 100%, either with manual back-blotting for 5-7s and a drain
607 time of 1s or using the automatic blotting function of the Vitrobot with a wait time of 10s, blot
608 time of 5-6s, blot force of 3 and drain time of 1s.

609

610 FIB milling

611 Grids were clipped in Autogrid holders (*Thermo Fisher*) machined with a notch to allow FIB
612 milling closer to the edge of the grid. Autogrids were placed in a custom-built shuttle and
613 inserted into a Versa 3D dual-beam FIB/SEM microscope with FEG (*FEI*) equipped with a
614 PP3000T cryo-transfer apparatus (*Quorum Technologies*). They were maintained at -175°C at
615 all times by a custom-built cryo-stage⁸⁵. To reduce sample charging and protect the sample
616 from curtaining during milling, the grids were sputter-coated with platinum at 15 mA for 60
617 seconds. Thin lamellae were generated with the Ga⁺ ion beam at 30 kV at angles ranging from
618 10 to 17 degrees. Rough milling was done at high currents, ranging from 0.3 nA to 100 pA until
619 the lamellae measured 1 micron in thickness under the FIB view. Current was then
620 progressively brought down to 10 pA for the final milling steps until the measured thickness
621 was between 100-200 nm. Final polishing of the back end of the lamella is also done at 10pA

622 where the sample is tilted +0.5 to 1° to homogenize the lamella thickness. During the whole
623 procedure, imaging with the SEM beam was done at 5 kV and 13 pA.

624

625 Electron cryo-tomography

626 Tomography of whole cells and FIB-milled lamellae was performed on either a Titan Krios or
627 Tecnai G2 Polara transmission electron microscope (*Thermo Fisher*) equipped with 300 kV
628 field emission gun, energy filter (*Gatan*) and K2 or K3 Summit direct electron detector (*Gatan*).
629 The Krios is equipped with a Volta phase plate (*Thermo Fisher*)⁸⁶. Tilt-series acquisition was
630 done with SerialEM⁸⁷ with a 2-3° tilt increment for a total range of ±60° or ±50°, defocus of -
631 4, -6 or -8 μm, and total dose up to 180 e⁻/Å². Volta phase plate imaging was performed in
632 Figures 1, 2, 5 and 7A-B with a defocus of -2μm and a measured phase shift of 0.5 π/rad before
633 tilt series acquisitions.

634

635 Low magnification tomography on the biofilm lamellae was performed at 6500 magnification
636 (14 Å² pixel size) with a -10 or -15 μm defocus and a total dose between 5 and 10 e⁻/Å².
637 Tomography of FIB-milled lamellae was done exclusively on the Titan Krios. Because samples
638 were thinner, the total dose was limited to ~80 e⁻/Å².

639

640 Data processing

641 Tomograms were reconstructed using the IMOD software (<http://bio3d.colorado.edu/imod/>)⁸⁸.
642 Alignment was done on 1k x 1k binned tilt-series with fiducial-based alignment. Aligned stacks
643 were low-pass filtered (0.35, σ = 0.05) to eliminate high-frequency noise. Weighted back
644 projection reconstruction was performed and the “SIRT-like filter” was used with 20 iterations.
645 Segmentation was also done using IMOD and drawing tools developed by Andrew Noske
646 (<http://www.andrewnoske.com/student/imod.php>). To better distinguish features during the

647 segmentation steps, tomograms were filtered with the 3D non-linear anisotropic diffusion filter
648 in IMOD. The cell contours and cortical belt were segmented manually on a Cintiq 21uX tablet
649 (*Wacom*) and cellulose was segmented using a semi-automated thresholded method. 1) A
650 denoising Non-linear Anisotropic Diffusion filter was applied (included in the *etomo* package,
651 <http://bio3d.colorado.edu/imod/>) on the tomogram; 2) Precise boundary models are drawn
652 around the structures to be thresholded; 3) Thresholding segmentation is performed with
653 3Dmod using the isosurface function and the previously drawn contours are used as a mask.
654 When the contours are precisely following the contours, this technic allows to raise the
655 isosurface threshold without picking up background noise.

656 Measurements for all distances between elements (cellulose sheet – outer-membrane, width of
657 the cellulose ribbon, cortical belt – inner-membrane) were taken by generating normalized
658 density profile plots and measuring the distances between the density peaks of the
659 corresponding sub-cellular features (Fig. 3). This was automated with a custom script, *sideview-*
660 *profile-average*, written by Davi Ortega ([https://www.npmjs.com/package/sideview-profile-](https://www.npmjs.com/package/sideview-profile-average)
661 [average](https://www.npmjs.com/package/sideview-profile-average)).

662
663 Estimation of the cell depth in the native biofilm lamellae was calculated as follows: 1) using
664 the two parallel walls of the milled trench, a perpendicular line is traced at the leading edge of
665 the lamella (where the platinum meets the frozen material); 2) Lines are drawn from the center
666 of the cells to the leading edge perpendicular line (Fig. 6H, red line in top view of lamella); 3)
667 The distance from the cell center to the limit of the platinum on the leading edge, which is the
668 surface of the sample, is measured. The real depth is then calculated using the following
669 equation: opposite side (real depth) = $\tan(a)$ x adjacent side (distance measured, d in Fig. 6H).
670 The angle a is the angle between the grid surface and the FIB gun during the milling process,
671 which can be accurately measured during reconstruction with 3dmod.

672

673 Statistical analysis

674 All statistics were performed with GraphPad Prism software
675 (<https://www.graphpad.com/scientific-software/prism/>). All datasets were first analyzed for
676 normality using the Shapiro-Wilk test and homoscedasticity (equal standard deviations). If
677 dataset is normal, appropriate parametric tests were performed and if not, appropriate non-
678 parametric tests were performed. Detailed statistical tests are listed in order of appearance in
679 the manuscript.

680

681 **Figure 2E:** n = 3 and 23 for the “loose” and “tight” configuration respectively. Two tailed P-
682 value = 0.0008, Mann-Whitney test.

683 **OM-to-closest-sheet distance in 20min vs 300min post separation cells:** n = 4, 2, 23 and 3
684 for 20min “tight”, 20min “loose”, 300min “tight” and 300min “loose” configurations,
685 respectively. Kruskal Wallis test followed by Dunn’s multiple comparison test was performed.
686 20min “tight” vs 20min “loose”, 300min “tight” and “loose” showed adjusted P-values of 0.12,
687 >0.99 and 0.024, respectively. 20min “loose” vs 300min “tight”, “loose” and 300min “tight” vs
688 300min “loose” showed adjusted P-values of 0.23, >0.99 and 0.032, respectively.

689 **Figure 4A:** n = 6, 15, 33 for 13-, 20- and 300-minutes, respectively.

690 **Figure 4B:** n = 6 and n = 21 tomograms for 20- and 300-minutes post-separation, respectively.
691 Two tailed P-value < 0.0001, One sample Wilcoxon signed rank test against a theoretical value
692 of 1 (number of sheets observed at 20-min post-separation).

693 **Figure 4H:** n = 12 and 4 microfibril thickness measurements performed on two separate
694 tomograms (Cell #1 and #2, left side of the graph). N = 47 measurements for inter-sheet
695 distances performed on 23 tomograms. ANOVA followed by Tukey’s multiple comparison test

696 was performed. Cell #1 vs Cell #2, Cell #1 vs 300-min inter-sheet distances and Cell #2 vs 300-
697 min inter-sheet distances showed adjusted P-values of 0.073, 0.15 and 0.0015, respectively.

698 **Figure 4I:** n = 6 and 45 sheets measured at 20- and 300-minutes post-separation. Welch's t test
699 (parametric t-test without equal SD assumption) showed a P-value of 0.23.

700 **Figure 6F:** n = 6 and 4 for biofilms let to grow for 3h and 6h, respectively. Unpaired T-test
701 showed a two-tailed P-value of 0.0011.

702 **Figure 6G:** n = 6 and 4 for biofilms let to grow for 3h and 6h, respectively. Unpaired T-test
703 showed a two-tailed P-value of 0.2720.

704 **Figure 6H:** n = 49, 46, 4 and 11 for live and dead cells in 3h and 6h biofilms, respectively.
705 Mann-Whitney tests were performed on live vs dead cells in 3h and 6h biofilms conditions,
706 showing two-tailed P-values of 0.82 and 0.54, respectively.

707 **G. hansenii cellulose sheet width versus A. tumefaciens cellulose fibrils width:** n = 52, 45
708 and 6 width measurements on A. tumefaciens, G. hansenii 20-min and 300-min post-separation,
709 respectively. Kruskal-Wallis one-way analysis of variance followed by Dunn's multiple
710 comparisons test was performed. T-20min vs t-300min, t-20min vs A. tumefaciens and t-
711 300min vs A. tumefaciens showed adjusted P-values of 0.25, 0.11 and <0.0001, respectively.

712

713 **Bibliography**

714 1. Pauly, Markus & Keestra, Kenneth. Cell-wall carbohydrates and their modification as
715 a resource for biofuels. *Plant Journal* vol. 54 559–568 (2008).

716 2. Pauly, Markus & Keestra, Kenneth. Plant cell wall polymers as precursors for
717 biofuels. *Current Opinion in Plant Biology* vol. 13 305–312 (2010).

718 3. Hon, David N. S. Cellulose: a random walk along its historical path. *Cellulose* **1**, 1–25
719 (1994).

720 4. Xu, Youjie, Zhang, Meng, Roozeboom, Kraig & Wang, Donghai. Integrated bioethanol

- 721 production to boost low-concentrated cellulosic ethanol without sacrificing ethanol
722 yield. *Bioresour. Technol.* **250**, 299–305 (2018).
- 723 5. Gatenholm, Paul & Klemm, Dieter. Bacterial Nanocellulose as a Renewable Material
724 for Biomedical Applications. *MRS Bull.* **35**, 208–213 (2010).
- 725 6. Cavalcante, Aline Ribeiro Teixeira, Lima, Rodrigo Pontes de, Souza, Veridiana Sales
726 Barbosa de, Pinto, Flávia Cristina Morone, Campos Júnior, Olavio, Silva, Jaiurte
727 Gomes Martins da, Albuquerque, Amanda Vasconcelos de & Aguiar, José Lamartine
728 de Andrade. Effects of bacterial cellulose gel on the anorectal resting pressures in rats
729 submitted to anal sphincter injury. *Heliyon* **4**, e01058 (2018).
- 730 7. Brown Jr., R. M. The biosynthesis of cellulose. *J. Macromol. Sci. Part A Pure Appl.*
731 *Chem.* **33**, 1345–1373 (1996).
- 732 8. McNamara, Joshua T., Morgan, Jacob L. W. & Zimmer, Jochen. A molecular
733 description of cellulose biosynthesis. *Annu. Rev. Biochem.* **84**, 895–921 (2015).
- 734 9. Kubicki, James D., Yang, Hui, Sawada, Daisuke, O'Neill, Hugh, Oehme, Daniel &
735 Cosgrove, Daniel. The Shape of Native Plant Cellulose Microfibrils. *Sci. Rep.* **8**, 1–8
736 (2018).
- 737 10. Cousins, Susan K. & Brown, R. Malcolm. Cellulose I microfibril assembly:
738 computational molecular mechanics energy analysis favours bonding by van der Waals
739 forces as the initial step in crystallization. *Polymer* **36**, 3885–3888 (1995).
- 740 11. Nishiyama, Yoshiharu, Langan, Paul & Chanzy, Henri. Crystal structure and hydrogen-
741 bonding system in cellulose I β from synchrotron X-ray and neutron fiber diffraction. *J.*
742 *Am. Chem. Soc.* **124**, 9074–9082 (2002).
- 743 12. Nishiyama, Yoshiharu, Sugiyama, Junji, Chanzy, Henri & Langan, Paul. Crystal
744 Structure and Hydrogen Bonding System in Cellulose I α from Synchrotron X-ray and
745 Neutron Fiber Diffraction. *J. Am. Chem. Soc.* **125**, 14300–14306 (2003).

- 746 13. Cosgrove, Daniel J. Growth of the plant cell wall. *Nat. Rev. Mol. Cell Biol.* **6**, 850–861
747 (2005).
- 748 14. Flemming, Hans Curt, Wingender, Jost, Szewzyk, Ulrich, Steinberg, Peter, Rice, Scott
749 A. & Kjelleberg, Staffan. Biofilms: An emergent form of bacterial life. *Nature Reviews*
750 *Microbiology* vol. 14 563–575 (2016).
- 751 15. Römling, Ute & Galperin, Michael Y. Bacterial cellulose biosynthesis: Diversity of
752 operons, subunits, products, and functions. *Trends in Microbiology* vol. 23 545–557
753 (2015).
- 754 16. De Vos, Willem M. Microbial biofilms and the human intestinal microbiome. *npj*
755 *Biofilms and Microbiomes* vol. 1 15005 (2015).
- 756 17. Costerton, J. W., Cheng, K. J., Geesey, G. G., Ladd, T. I., Nickel, J. C., Dasgupta, M.
757 & Marrie, T. J. Bacterial Biofilms in Nature and Disease. *Annu. Rev. Microbiol.* **41**,
758 435–464 (1987).
- 759 18. Haigler, Candace Hope, Brown, R. Malcolm & Benziman, Moshe. Calcofluor White
760 ST Alters the in vivo Assembly of Cellulose Microfibrils. *Science* **119**, 80–82 (1980).
- 761 19. Morgan, Jacob L. W., McNamara, Joshua T., Fischer, Michael, Rich, Jamie, Chen,
762 Hong Ming, Withers, Stephen G. & Zimmer, Jochen. Observing cellulose biosynthesis
763 and membrane translocation in crystallo. *Nature* **531**, 329–334 (2016).
- 764 20. Du, Juan, Vepachedu, Venkata, Cho, Sung Hyun, Kumar, Manish & Nixon, B. Tracy.
765 Structure of the cellulose synthase complex of *Gluconacetobacter hansenii* at 23.4 Å
766 resolution. *PLoS One* **11**, e0155886 (2016).
- 767 21. Hu, S. Q., Gao, Y. G., Tajima, Kenji, Sunagawa, Naoki, Zhou, Yong, Kawano, Shin,
768 Fujiwara, Takaaki, Yoda, Takanori, Shimura, Daisuke, Satoh, Yasuharu, Munekata,
769 Masanobu, Tanaka, Isao & Yao, Min. Structure of bacterial cellulose synthase subunit
770 D octamer with four inner passageways. *Proc. Natl. Acad. Sci.* **107**, 17957–17961

- 771 (2010).
- 772 22. Iyer, Prashanti R., Catchmark, Jeffrey, Brown, Nicole R. & Tien, Ming. Biochemical
773 localization of a protein involved in synthesis of *Gluconacetobacter hansenii* cellulose.
774 *Cellulose* **18**, 739–747 (2011).
- 775 23. Saxena, I. M., Kudlicka, K., Okuda, K. & Brown, R. M. Characterization of genes in
776 the cellulose-synthesizing operon (acs operon) of *Acetobacter xylinum*: Implications
777 for cellulose crystallization. *J. Bacteriol.* **176**, 5735–5752 (1994).
- 778 24. Acheson, Justin F., Derewenda, Zygmunt S. & Zimmer, Jochen. Architecture of the
779 Cellulose Synthase Outer Membrane Channel and Its Association with the Periplasmic
780 TPR Domain. *Structure* **27**, 1855-1861.e3 (2019).
- 781 25. Whitney, John C., Hay, Iain D., Li, Canhui, Eckford, Paul D. W., Robinson, Howard,
782 Amaya, Maria F., Wood, Lynn F., Ohman, Dennis E., Bear, Christine E., Rehm, Bernd
783 H. & Lynne Howell, P. Structural basis for alginate secretion across the bacterial outer
784 membrane. *Proc. Natl. Acad. Sci.* **108**, 13083–13088 (2011).
- 785 26. Rehman, Zahid U., Wang, Yajie, Moradali, M. Fata, Hay, Iain D. & Rehm, Bernd H.
786 A. Insights into the assembly of the alginate biosynthesis machinery in *Pseudomonas*
787 *aeruginosa*. *Appl. Environ. Microbiol.* **79**, 3264–3272 (2013).
- 788 27. Keiski, Carrie-Lynn, Harwich, Michael, Jain, Sumita, Neculai, Ana Mirela, Yip,
789 Patrick, Robinson, Howard, Whitney, John C., Riley, Laura, Burrows, Lori L., Ohman,
790 Dennis E. & Howell, P. Lynne. AlgK Is a TPR-Containing Protein and the Periplasmic
791 Component of a Novel Exopolysaccharide Secretin. *Structure* **18**, 265–273 (2010).
- 792 28. Haigler, Candace Hope. Alteration of cellulose assembly in *Acetobacter xylinum* by
793 fluorescenet brightening agents, direct dyes and cellulose derivatives. (University of
794 North Carolina, 1982).
- 795 29. Mehta, Kalpa, Pfeffer, Sarah & Brown, R. Malcolm. Characterization of an acsD

- 796 disruption mutant provides additional evidence for the hierarchical cell-directed self-
797 assembly of cellulose in *Gluconacetobacter xylinus*. *Cellulose* **22**, 119–137 (2015).
- 798 30. Nakai, Tomonori, Sugano, Yasushi, Shoda, Makoto, Sakakibara, Hitoshi, Oiwa,
799 Kazuhiro, Tuzi, Satoru, Imai, Tomoya, Sugiyama, Junji, Takeuchi, Miyuki, Yamauchi,
800 Daisuke & Mineyukia, Yoshinobu. Formation of highly twisted ribbons in a
801 carboxymethylcellulase gene-disrupted strain of a cellulose-producing bacterium. *J.*
802 *Bacteriol.* **195**, 958–964 (2013).
- 803 31. Sunagawa, Naoki, Fujiwara, Takaaki, Yoda, Takanori, Kawano, Shin, Satoh,
804 Yasuharu, Yao, Min, Tajima, Kenji & Dairi, Tohru. Cellulose complementing factor
805 (Ccp) is a new member of the cellulose synthase complex (terminal complex) in
806 *Acetobacter xylinum*. *J. Biosci. Bioeng.* **115**, 607–612 (2013).
- 807 32. Deng, Ying, Nagachar, Nivedita, Xiao, Chaowen, Tien, Ming & Kao, Teh Hui.
808 Identification and characterization of non-cellulose-producing mutants of
809 *Gluconacetobacter hansenii* generated by Tn5 transposon mutagenesis. *J. Bacteriol.*
810 **195**, 5072–5083 (2013).
- 811 33. Haigler, Candace H. & Benziman, Moshe. Biogenesis of Cellulose I Microfibrils
812 Occurs by Cell-Directed Self-Assembly in *Acetobacter xylinum*. in *Cellulose and*
813 *Other Natural Polymer Systems* 273–297 (Springer US, 1982).
- 814 34. Cousins, Susan K. & Brown, R. Malcolm. Photoisomerization of a dye-altered β -1,4
815 glucan sheet induces the crystallization of a cellulose-composite. *Polymer* **38**, 903–912
816 (1997).
- 817 35. Toyosaki, HIROSHI, KOJIMA, Yukiko, Tsuchida, TAKAYASU, HOSHINO, Ken-
818 Ichiro, YAMADA, Yuzo & Yoshinaga, FUMIHIRO. The characterization of an acetic
819 acid bacterium useful for producing bacterial cellulose in agitation cultures: The
820 proposal of *Acetobacter xylinum* subsp. *sucrofermentans* subsp. nov. *J. Gen. Appl.*

- 821 *Microbiol.* **41**, 307–314 (1995).
- 822 36. Park, Joong Kon, Jung, Jae Yong & Park, Youn Hee. Cellulose production by
823 *Gluconacetobacter hansenii* in a medium containing ethanol. *Biotechnol. Lett.* **25**,
824 2055–2059 (2003).
- 825 37. Schramm, M. & Hestrin, S. Factors affecting Production of Cellulose at the Air/ Liquid
826 Interface of a Culture of *Acetobacter xylinum*. *J. Gen. Microbiol.* **11**, 123–129 (1954).
- 827 38. Brown, R. M., Willison, J. H., Richardson, C. L. & Richardson, C. L. Cellulose
828 biosynthesis in *Acetobacter xylinum*: visualization of the site of synthesis and direct
829 measurement of the in vivo process. *Proc. Natl. Acad. Sci. U. S. A.* **73**, 4565–9 (1976).
- 830 39. Zaar, K. Visualization of pores (export sites) correlated with cellulose production in the
831 envelope of the gram-negative bacterium *Acetobacter xylinum*. *J. Cell Biol.* **80**, 773–
832 777 (1979).
- 833 40. Saxena, I. M. & Brown, R. M. Identification of a second cellulose synthase gene
834 (*acsAII*) in *Acetobacter xylinum*. *J. Bacteriol.* **177**, 5276–83 (1995).
- 835 41. Florea, Michael, Reeve, Benjamin, Abbott, James, Freemont, Paul S. & Ellis, Tom.
836 Genome sequence and plasmid transformation of the model high-yield bacterial
837 cellulose producer *Gluconacetobacter hansenii* ATCC 53582. *Sci. Rep.* **6**, 23635
838 (2016).
- 839 42. Palmer, Colin M. & Löwe, Jan. A cylindrical specimen holder for electron cryo-
840 tomography. *Ultramicroscopy* **137**, 20–29 (2014).
- 841 43. Hawkes, Peter W. The electron microscope as a structure projector. in *Electron*
842 *Tomography: Methods for Three-Dimensional Visualization of Structures in the Cell*
843 vol. 9780387690087 83–111 (Springer New York, 2006).
- 844 44. Radermacher, Michael. Weighted back-projection methods. in *Electron Tomography:*
845 *Methods for Three-Dimensional Visualization of Structures in the Cell* vol.

- 846 9780387690087 245–273 (Springer New York, 2006).
- 847 45. Dobro, Megan J., Oikonomou, Catherine M., Piper, Aidan, Cohen, John, Guo, Kylie,
848 Jensen, Taylor, Tadayon, Jahan, Donermeyer, Joseph, Park, Yeram, Solis, Benjamin
849 A., Kjær, Andreas, Jewett, Andrew I., McDowall, Alasdair W., Chen, Songye, Chang,
850 Yi-Wei, Shi, Jian, Subramanian, Poorna, Iancu, Cristina V, Li, Zhuo, Briegel, Ariane,
851 Tocheva, Elitza I., Pilhofer, Martin & Jensen, Grant J. Uncharacterized Bacterial
852 Structures Revealed by Electron Cryotomography. *J. Bacteriol.* **199**, e00100-17 (2017).
- 853 46. Ryngajłło, Małgorzata, Jędrzejczak-Krzepkowska, Marzena, Kubiak, Katarzyna,
854 Ludwicka, Karolina & Bielecki, Stanisław. Towards control of cellulose biosynthesis
855 by *Komagataeibacter* using systems-level and strain engineering strategies: current
856 progress and perspectives. *Appl. Microbiol. Biotechnol.* 1–21 (2020)
857 doi:10.1007/s00253-020-10671-3.
- 858 47. Le Quéré, Benjamin & Ghigo, Jean Marc. BcsQ is an essential component of the
859 *Escherichia coli* cellulose biosynthesis apparatus that localizes at the bacterial cell pole.
860 *Mol. Microbiol.* **72**, 724–740 (2009).
- 861 48. Matthyse, A. G., Holmes, K. V & Gurlitz, R. H. G. Elaboration of cellulose fibrils by
862 *Agrobacterium tumefaciens* during attachment to carrot cells. *J. Bacteriol.* **145**, 583–
863 595 (1981).
- 864 49. Xu, Jing, Kim, Jinwoo, Koestler, Benjamin J., Choi, Jeong Hyeon, Waters, Christopher
865 M. & Fuqua, Clay. Genetic analysis of *agrobacterium tumefaciens* unipolar
866 polysaccharide production reveals complex integrated control of the motile-to-sessile
867 switch. *Mol. Microbiol.* **89**, 929–948 (2013).
- 868 50. Ross, Peter, Mayer, Raphael, Benziman, A. N. D. Moshe & Benziman, M. Cellulose
869 Biosynthesis and Function in Bacteria. *Microbiology* **55**, 35–58 (1991).
- 870 51. Benziman, Moshe, Haigler, Candace H., Brown, R. Malcolm, White, Alan R. &

- 871 Cooper, Kay M. Cellulose biogenesis: Polymerization and crystallization are coupled
872 processes in *Acetobacter xylinum*. *Proc. Natl. Acad. Sci. U. S. A.* **77**, 6678–6682
873 (1980).
- 874 52. Yasutake, Yoshiaki, Kawano, Shin, Tajima, Kenji, Yao, Min, Satoh, Yasuharu,
875 Munekata, Masanobu & Tanaka, Isao. Structural characterization of the *Acetobacter*
876 *xylinum* endo- β -1,4-glucanase CMCax required for cellulose biosynthesis. *Proteins*
877 *Struct. Funct. Bioinforma.* **64**, 1069–1077 (2006).
- 878 53. Dohnalkova, Alice C., Marshall, Matthew J., Arey, Bruce W., Williams, Kenneth H.,
879 Buck, Edgar C. & Fredrickson, James K. Imaging hydrated microbial extracellular
880 polymers: Comparative analysis by electron microscopy. *Appl. Environ. Microbiol.* **77**,
881 1254–1262 (2011).
- 882 54. White, Alan R. & Brown, R. M. Enzymatic hydrolysis of cellulose: Visual
883 characterization of the process. *Proc. Natl. Acad. Sci. U. S. A.* **78**, 1047–1051 (1981).
- 884 55. Kimura, S., Chen, H. P., Saxena, I. M., Brown, Jr & Itoh, T. Localization of c-di-GMP-
885 binding protein with the linear terminal complexes of *Acetobacter xylinum*. *J.*
886 *Bacteriol.* **183**, 5668–5674 (2001).
- 887 56. Matthyse, Ann G., White, Sally & Lightfoot, Richard. Genes required for cellulose
888 synthesis in *Agrobacterium tumefaciens*. *J. Bacteriol.* **177**, 1069–1075 (1995).
- 889 57. Deng, Ying, Nagachar, Nivedita, Fang, Lin, Luan, Xin, Catchmark, Jeffrey M., Tien,
890 Ming & Kao, Teh Hui. Isolation and characterization of two cellulose morphology
891 mutants of *Gluconacetobacter hansenii* ATCC23769 producing cellulose with lower
892 crystallinity. *PLoS One* **10**, e0119504 (2015).
- 893 58. Krasteva, Petya Violinova, Bernal-Bayard, Joaquin, Travier, Laetitia, Martin, Fernando
894 Ariel, Kaminski, Pierre Alexandre, Karimova, Gouzel, Fronzes, Rémi & Ghigo, Jean
895 Marc. Insights into the structure and assembly of a bacterial cellulose secretion system.

- 896 *Nat. Commun.* **8**, 2065 (2017).
- 897 59. Pilhofer, Martin & Jensen, Grant J. *The bacterial cytoskeleton: More than twisted*
898 *filaments. Current Opinion in Cell Biology* vol. 25 1–9 (2013).
- 899 60. Kühn, Juliane, Briegel, Ariane, Mörschel, Erhard, Kahnt, Jörg, Leser, Katja, Wick,
900 Stephanie, Jensen, Grant J. & Thanbichler, Martin. Bactofilins, a ubiquitous class of
901 cytoskeletal proteins mediating polar localization of a cell wall synthase in *Caulobacter*
902 *crescentus*. *EMBO J.* **29**, 327–339 (2010).
- 903 61. Ingerson-Mahar, Michael, Briegel, Ariane, Werner, John N., Jensen, Grant J. & Gitai,
904 Zemer. The metabolic enzyme CTP synthase forms cytoskeletal filaments. *Nat. Cell*
905 *Biol.* **12**, 739–746 (2010).
- 906 62. Pear, J. R., Kawagoe, Y., Schreckengost, W. E., Delmer, D. P. & Stalker, D. M. Higher
907 plants contain homologs of the bacterial *celA* genes encoding the catalytic subunit of
908 cellulose synthase. *Proc. Natl. Acad. Sci. U. S. A.* **93**, 12637–42 (1996).
- 909 63. Nobles, David R. & Brown, R. Malcolm. The pivotal role of cyanobacteria in the
910 evolution of cellulose synthases and cellulose synthase-like proteins. *Cellulose* **11**,
911 437–448 (2004).
- 912 64. Nobles, D. R., Romanovicz, D. K. & Brown, Jr. Cellulose in cyanobacteria. Origin of
913 vascular plant cellulose synthase? *Plant Physiol.* **127**, 529–542 (2001).
- 914 65. Lampugnani, Edwin R., Flores-Sandoval, Eduardo, Tan, Qiao Wen, Mutwil, Marek,
915 Bowman, John L. & Persson, Staffan. Cellulose Synthesis – Central Components and
916 Their Evolutionary Relationships. *Trends in Plant Science* vol. 24 402–412 (2019).
- 917 66. Diotallevi, Fabiana & Mulder, Bela. The cellulose synthase complex: A polymerization
918 driven supramolecular motor. *Biophys. J.* **92**, 2666–2673 (2007).
- 919 67. Chan, Jordi, Coen, Enrico, Chan, Jordi & Coen, Enrico. Interaction between
920 Autonomous and Microtubule Guidance Systems Controls Cellulose Synthase Report

- 921 Interaction between Autonomous and Microtubule Guidance Systems Controls
922 Cellulose Synthase Trajectories. *Curr. Biol.* 1–7 (2020).
- 923 68. Paredez, Alexander R., Somerville, Christopher R. & Ehrhardt, David W. Visualization
924 of cellulose synthase demonstrates functional association with microtubules. *Science*
925 **312**, 1491–1495 (2006).
- 926 69. Li, Shundai, Lei, Lei, Somerville, Christopher R. & Gu, Ying. Cellulose synthase
927 interactive protein 1 (CSI1) mediates the intimate relationship between cellulose
928 microfibrils and cortical microtubules. *Plant Signal. Behav.* **7**, 1–5 (2012).
- 929 70. Sampathkumar, Arun, Peaucelle, Alexis, Fujita, Miki, Schuster, Christoph, Persson,
930 Staffan, Wasteneys, Geoffrey O. & Meyerowitz, Elliot M. Primary wall cellulose
931 synthase regulates shoot apical meristem mechanics and growth. *Development* **146**,
932 (2019).
- 933 71. Fujita, Miki, Himmelspach, Regina, Ward, Juliet, Whittington, Angela, Hasenbein,
934 Nortrud, Liu, Christine, Truong, Thy T., Galway, Moira E., Mansfield, Shawn D.,
935 Hocart, Charles H. & Wasteneys, Geoffrey O. The anisotropy1 D604N mutation in the
936 Arabidopsis cellulose synthase1 catalytic domain reduces cell wall crystallinity and the
937 velocity of cellulose synthase complexes. *Plant Physiol.* **162**, 74–85 (2013).
- 938 72. Fujita, Miki, Himmelspach, Regina, Hocart, Charles H., Williamson, Richard E.,
939 Mansfield, Shawn D. & Wasteneys, Geoffrey O. Cortical microtubules optimize cell-
940 wall crystallinity to drive unidirectional growth in Arabidopsis. *Plant J.* **66**, 915–928
941 (2011).
- 942 73. Liu, Zengyu, Schneider, Rene, Kesten, Christopher, Zhang, Youjun Yi, Somssich,
943 Marc, Zhang, Youjun Yi, Fernie, Alisdair R. & Persson, Staffan. Cellulose-
944 Microtubule Uncoupling Proteins Prevent Lateral Displacement of Microtubules during
945 Cellulose Synthesis in Arabidopsis. *Dev. Cell* **38**, 305–315 (2016).

- 946 74. Standal, R., Iversen, T. G., Coucheron, D. H., Fjaervik, E., Blatny, J. M. & Valla, S. A
947 new gene required for cellulose production and a gene encoding cellulolytic activity in
948 *Acetobacter xylinum* are colocalized with the *bcs* operon. *J. Bacteriol.* **176**, 665–672
949 (1994).
- 950 75. López, Daniel, Vlamakis, Hera, Losick, Richard & Kolter, Roberto. Cannibalism
951 enhances biofilm development in *Bacillus subtilis*. *Mol. Microbiol.* **74**, 609–618 (2009).
- 952 76. Billings, Nicole, Birjiniuk, Alona, Samad, Tahoura S., Doyle, Patrick S. & Ribbeck,
953 Katharina. Material properties of biofilms - A review of methods for understanding
954 permeability and mechanics. *Reports Prog. Phys.* **78**, (2015).
- 955 77. Stewart, Philip S. Diffusion in biofilms. *Journal of Bacteriology* vol. 185 1485–1491
956 (2003).
- 957 78. Xu, Karen D., Stewart, Philip S., Xia, Fuhu, Huang, Ching Tsan & McFeters, Gordon
958 A. Spatial physiological heterogeneity in *Pseudomonas aeruginosa* biofilm is
959 determined by oxygen availability. *Appl. Environ. Microbiol.* **64**, 4035–4039 (1998).
- 960 79. Jo, Jeanyoung, Cortez, Krista L., Cornell, William Cole, Price-Whelan, Alexa &
961 Dietrich, Lars E. P. An orphan *cbb3*-type cytochrome oxidase subunit supports
962 *Pseudomonas aeruginosa* biofilm growth and virulence. *Elife* **6**, (2017).
- 963 80. Sartori, N., Richter, Karsten & Dubochet, Jacques. Vitrification depth can be increased
964 more than 10-fold by high-pressure freezing. *J. Microsc.* **172**, 55–61 (1993).
- 965 81. Harapin, Jan, Börmel, Mandy, Sapra, K. Tanuj, Brunner, Damian, Kaech, Andres &
966 Medalia, Ohad. Structural analysis of multicellular organisms with cryo-electron
967 tomography. *Nat. Methods* (2015).
- 968 82. Hsieh, Chyongere, Schmelzer, Thomas, Kishchenko, Gregory, Wagenknecht, Terence
969 & Marko, Michael. Practical workflow for cryo focused-ion-beam milling of tissues
970 and cells for cryo-TEM tomography. *J. Struct. Biol.* **185**, 32–41 (2014).

- 971 83. Schaffer, Miroslava, Pfeffer, Stefan, Mahamid, Julia, Kleindiek, Stephan, Laugks, Tim,
972 Albert, Sahrada, Engel, Benjamin D., Rummel, Andreas, Smith, Andrew J.,
973 Baumeister, Wolfgang & Plitzko, Juergen M. A cryo-FIB lift-out technique enables
974 molecular-resolution cryo-ET within native *Caenorhabditis elegans* tissue. *Nat.*
975 *Methods* **16**, 757–762 (2019).
- 976 84. Das, Aditi & Das, Anath. Delineation of polar localization domains of *Agrobacterium*
977 *tumefaciens* type IV secretion apparatus proteins VirB4 and VirB11. *Microbiologyopen*
978 **3**, 793–802 (2014).
- 979 85. Rigort, Alexander, Bäuerlein, Felix J. B., Leis, Andrew, Gruska, Manuela, Hoffmann,
980 Christian, Laugks, Tim, Böhm, Ulrike, Eibauer, Matthias, Gnaegi, Helmut, Baumeister,
981 Wolfgang & Plitzko, Jürgen M. Micromachining tools and correlative approaches for
982 cellular cryo-electron tomography. *J. Struct. Biol.* **172**, 169–179 (2010).
- 983 86. Danev, Radostin, Buijsse, Bart, Khoshouei, Maryam, Plitzko, Jürgen M. & Baumeister,
984 Wolfgang. Volta potential phase plate for in-focus phase contrast transmission electron
985 microscopy. *Proc. Natl. Acad. Sci. U. S. A.* **111**, 15635–40 (2014).
- 986 87. Mastronarde, David N. Automated electron microscope tomography using robust
987 prediction of specimen movements. *J. Struct. Biol.* **152**, 36–51 (2005).
- 988 88. Kremer, J. R., Mastronarde, D. N. & McIntosh, J. R. Computer visualization of three-
989 dimensional image data using IMOD. *J. Struct. Biol.* **116**, 71–6 (1996).
- 990 89. Chang, Yi Wei, Rettberg, Lee A., Treuner-Lange, Anke, Iwasa, Janet, Sogaard-
991 Andersen, Lotte & Jensen, Grant J. Architecture of the type IVa pilus machine. *Science*
992 **351**, (2016).
- 993 90. Kaplan, Mohammed, Ghosal, Debnath, Subramanian, Poorna, Oikonomou, Catherine
994 M., Kjaer, Andreas, Pirbadian, Sahand, Ortega, Davi R., Briegel, Ariane, El-Naggat,
995 Mohamed Y. & Jensen, Grant J. The presence and absence of periplasmic rings in

996 bacterial flagellar motors correlates with stator type. *Elife* **8**, (2019).

997

998

999

1000

1001

1002 **Figures**

1003 **Figure 1 | Interactions between the bacterial envelope and the cellulose ribbon: the “tight”**
1004 **configuration**

1005 (A) Confocal-Airy scan optical slices show representative examples of *G. hansenii* cells in red
1006 (MitoTracker Deep Red FM) displaying the cellulose ribbon on their side in cyan (Calcofluor-
1007 white). (B) Enlarged view indicated by white dashed rectangle in (A). The cellulose structure
1008 is clearly seen closely appended to one side of the cell (cyan arrowheads). (C) 9-nm thick
1009 tomographic slice showing the typical *G. hansenii* cell harboring the cellulose ribbon on its
1010 right side (yellow arrows). White arrowheads point to ribosomes and red arrows point to
1011 cytosolic vesicles. Here and below, IM: Inner-membrane; OM: Outer-membrane; S: Storage
1012 granule; CB: Cortical belt. (D) Manual segmentation of the cell shown in (C). (E) Rotated
1013 segmented volume shown in (D) showing the very close contact between the cellulose ribbon
1014 (yellow) and the outer membrane (green). (F-H) Transverse 9-nm thick tomographic slices
1015 through the bacterial envelope of the cell shown in (C) at the levels indicated by the blue, black
1016 and red dashed lines, respectively. Two cellulose sheets (yellow arrows) are seen. One interacts
1017 with the OM all along (white arrow). Our working model is that integration of the cellulose
1018 fibers into the sheet occurs immediately upon secretion.

1019

1020 **Figure 2 | Interactions between the bacterial envelope and the cellulose ribbon: the “loose”**
1021 **configuration**

1022 (A) 9-nm thick tomographic slice showing a cell where aggregates of disorganized cellulose
1023 (orange asterisks) occur between the ribbon (yellow arrows) and the OM. Note the cortical belt
1024 (CB) cannot be seen in this slice. Black line orange arrows indicate points of contact between
1025 the cellulose sheet and the disorganized aggregates. Red arrows point to vesicles. (B) Manual
1026 segmentation of the tomogram in (A) showing these disorganized aggregates in 3-D. (C-D)
1027 Transverse 9-nm thick tomographic slices through the envelope of the cell shown in (A) at the
1028 levels indicated by the blue and pink dashed lines highlighting the distance between the two
1029 cellulose sheets (yellow arrows) and the OM and the presence of the disorganized clusters
1030 (orange dashed brackets). (E) Plot showing the OM-to-closest sheet distance in the two types
1031 of configuration. $n = 3$ and 23 for the “loose” and “tight” configuration respectively. Two tailed
1032 P-value = 0.0008 , Mann-Whitney test.

1034 **Figure 3 | Cellulose sheet dimensions**

1035 (A-B) Longitudinal and transverse schematic depiction defining the different dimensions
1036 measured, namely OM-to-sheet distance, sheet width and inter-sheet distance. Identical
1037 terminology is used for the measurements of the cortical belt. (C) Transverse 12-nm thick slice
1038 of the bacterial envelope of the cell shown in (D) at the level indicated by the blue dashed line.
1039 The yellow arrows highlight the two stacked sheets. On the right, the average density profile
1040 along the red line demonstrates how the cellulose sheet widths were estimated. Vertical axis is
1041 length in nm along the red line and horizontal axis is the normalized electron density. (D) 12-
1042 nm thick tomographic slice showing the typical organization of the bacterial envelope on the
1043 side where cellulose sheets (yellow arrows) are being synthesized. The average density profile

1044 on the right taken along the red line shows the CB-IM, IM-OM OM-sheet and inter-sheet
1045 distances (green dashed lines).

1046

1047 **Figure 4 | The cellulose ribbon is a composite structure made of stacked sheets**

1048 (A) Percentages of cells exhibiting disorganized aggregates (blue) and cellulose ribbons (red)
1049 at 13-, 20- and 300minutes post-separation. While disorganized aggregate occurrence is steady,
1050 there is an increase in the occurrence of cellulose ribbons over time. $n = 6, 15, 33$ for 13-, 20-
1051 and 300-minutes, respectively. (B) Number of cellulose sheets composing the ribbons as a
1052 function of time after cell separation. $n = 6$ and $n = 21$ tomograms for 20- and 300-minutes
1053 post-separation, respectively. Two tailed P-value < 0.0001 , One sample Wilcoxon signed rank
1054 test against a theoretical value of 1 (number of sheets observed at 20-min post-separation). (C)
1055 Composite image composed of 10-nm thick tomographic slices spaced by 24 nm in Z, of a cell
1056 20 minutes post separation in the “tight” configuration. The cellulose ribbon is thin (yellow
1057 arrows), composed of one sheet immediately adjacent to the OM. Limits of the two original
1058 images are indicated by the red dashed line. (D) 11 nm thick tomographic slice of a cell 300
1059 minutes post-separation. The cellulose ribbon (yellow arrows) is large and composed of
1060 multiple sheets. (E) Nascent cellulose sheet 20 minutes post-separation (yellow arrow). Putative
1061 microfibrils can be seen coming out perpendicularly from the outer membrane (red
1062 arrowheads). (F) Corresponding manual segmentation of (E). (G) Enlarged view of the blue
1063 boxed region in (E). Below is the average density profile showing the estimation of the diameter
1064 of one putative microfibril (red line). (H) Estimated diameters of microfibrils observed at 20-
1065 minutes post-separation in the two cells where they are visible (left vertical axis) as in (E) and
1066 the inter-sheet distances measured in the 300-minutes post-separation cellulose ribbons (right
1067 vertical axis). $n = 12$ and 4 microfibril thickness measurements performed on two separate
1068 tomograms (Cell #1 and #2, left side of the graph). $N = 47$ measurements for inter-sheet

1069 distances performed on 23 tomograms. ANOVA followed by Tukey's multiple comparison test
1070 was performed. Cell #1 vs Cell #2, Cell #1 vs 300-min inter-sheet distances and Cell #2 vs 300-
1071 min inter-sheet distances showed adjusted P-values of 0.073, 0.15 and 0.0015, respectively. **(I)**
1072 Sheet width estimations at 20- and 300-minutes post separation. n = 6 and 45 sheets measured
1073 at 20- and 300-minutes post-separation. Welch's t test (parametric t-test without equal SD
1074 assumption) showed a P-value of 0.23. **Figure 5 | The cortical belt lies below the cellulose**

1075 **ribbon in the cytoplasm**

1076 **(A)** 9-nm thick tomographic slice showing a representative cortical belt (purple arrows) just
1077 inside the IM and proximal to the cellulose ribbon on the outside of the cell (yellow arrows).
1078 **(B)** Manual segmentation of the tomogram shown in (A) highlighting the cellulose ribbon and
1079 the cortical belt. **(C)** Same segmentation rotated 90° about the long axis of the cell shows how
1080 the cortical belt and the cellulose ribbon follow the same trajectory. **(D)** 9-nm thick tomographic
1081 slice taken from the same tomogram as in figure 2, showing one out of several cases where the
1082 cortical belt presented stacked layers (red dashed box). **(E)** Enlarged view of the red dashed
1083 boxed region in (D) showing the arrangement of the stacked layers. On the right is a density
1084 profile displayed normal to the cortical belt to measure the inter-layer distance (15 nm). **(F)**
1085 Transverse 9-nm thick tomographic slice of the cell region shown in (D), at the level indicated
1086 by the blue dashed line, highlighting stacked layers of the cortical belt. The cellulose ribbon
1087 can be seen at a distance (yellow arrowheads) with disorganized aggregates in between (orange
1088 dashed brackets and asterisk).

1089

1090 **Figure 6 | FIB-milling through native *G. hansenii* biofilms**

1091 **(A)** cryo-SEM overview of a 6-hour biofilm (outlined in red) grown on a gold quantifoil grid.
1092 **(B)** cryo-SEM view of a thick biofilm area (boxed in blue in (A)). Wrinkles in the biofilm are
1093 typical of a biofilm a few microns thick. **(C)** Milled lamella (boxed in yellow) from the green

1094 boxed region shown in (A). (D) 23-nm thick tomographic slice of a low mag tomogram taken
1095 on the lamella shown in (C). Living (when frozen) and dead cells are visible (green and red
1096 asterisks, respectively) and large cellulose arrays can be seen filling the gaps between the cells
1097 (yellow arrowheads). (E) Manual segmentation of the tomogram shown in (D). (F) Fraction of
1098 the lamella volume occupied by the cells was assessed for each lamella. $n = 6$ and 4 for biofilms
1099 let to grow for 3h and 6h, respectively. Unpaired T-test showed a two-tailed P-value of 0.0011.
1100 (G) Live cell ratio in 3h and 6h biofilms. $n = 6$ and 4 for biofilms let to grow for 3h and 6h,
1101 respectively. Unpaired T-test showed a two-tailed P-value of 0.2720. (H) Violin boxplots
1102 reporting the absolute depth of the live and dead cells within the biofilms grown for 3 and 6
1103 hours. The dashed red lines indicate the first and third quartiles and solid red line represents
1104 median. This shows that while the biofilms get thicker with time, the ratio of live-to-dead cells
1105 appears constant through depth and time. Method of calculation is detailed on the left of the
1106 panel and in the methods section. Lamella is drawn in blue, with the platinum coated leading
1107 edge represented in gray. $n = 49, 46, 4$ and 11 for live and dead cells in 3h and 6h biofilms,
1108 respectively. Mann-Whitney tests were performed on live vs dead cells in 3h and 6h biofilms
1109 conditions, showing two-tailed P-values of 0.82 and 0.54, respectively.

1110

1111 **Figure 7 | Lamellae of native biofilms also reveal numerous vesicles and the cortical belt**

1112 (A-B) Two tomographic slices of a *G. hansenii* cell from a biofilm grown for 6h surrounded by
1113 cellulose ribbons (yellow arrowheads). The cortical belt is visible in (B) (purple arrow) and
1114 seems to follow the trajectory of the cellulose sheet proximal to the OM (dark lined yellow
1115 arrowhead). (C) Manual segmentation of the tomogram displayed in (A) and (B) showing the
1116 juxtaposition of the cortical belt (purple to red) and the nascent cellulose ribbon (yellow). (D)
1117 Enlargement of the boxed region in (B) showing the layered cortical belt. (E) Tomographic
1118 slice of a cell surrounded by cellulose ribbons (yellow arrowheads) from a biofilm grown for

1119 3h and harboring numerous vesicles in its cytosol (white arrowheads). Disorganized aggregates
1120 (orange dashed lines) are visible at this timepoint. **(F-G)** Tomographic slices showing
1121 additional examples of disorganized cellulose aggregates (orange dashed lines) surrounded by
1122 cellulose ribbons (yellow arrowheads) visible in 3h biofilms. Scale bars = 100 nm. All
1123 tomographic slices are 11-nm thick.

1124

1125 **Figure 8 | The cortical belt is not found in other cellulose-synthesizing species**

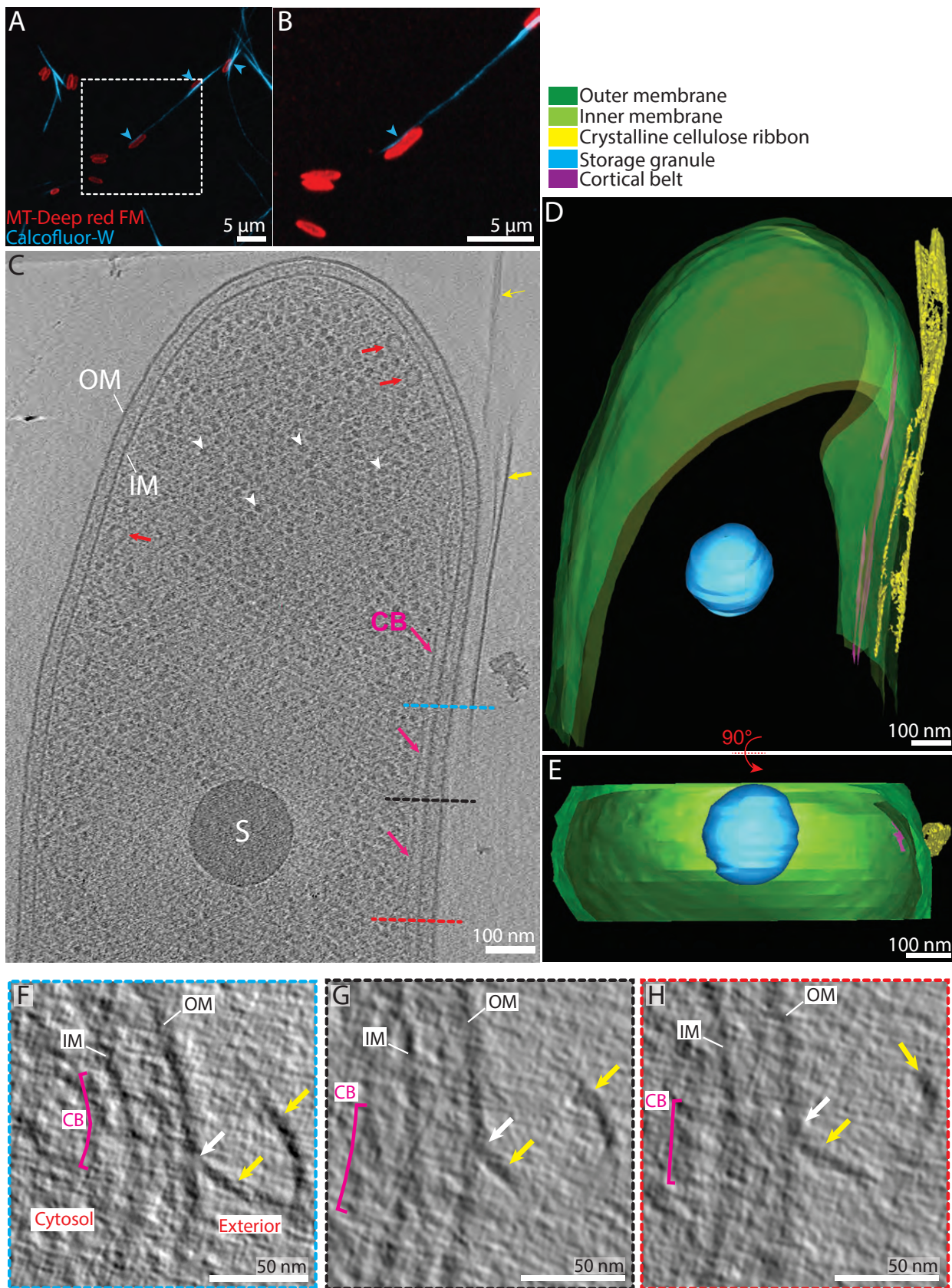
1126 **(A)** Maximum projection of *A. tumefaciens* cells synthesizing cellulose. Cells are stained with
1127 Mito Tracker Deep Red (red) and cellulose with Calcofluor-white (cyan). **(B)** 10-nm thick
1128 tomographic slice of a typical *A. tumefaciens* cell with cellulose microfibrils around (yellow
1129 arrowheads). No cortical belt can be seen in the cells. A polar flattening can be seen at the lower
1130 pole (cyan arrow) with an amorphous aggregate (orange dashed lines). These aggregates are
1131 most probably the UniPolar-Polysaccharide (UPP) synthesized specifically by *A. tumefaciens*.
1132 **(C)** Manual segmentation of the tomogram in (B) showing the organization of the cellulose
1133 microfibrils around the cell, the absence of the cortical belt and the putative UPP. **(D)** 50-nm
1134 optical slice of an induced *E. coli 1094* cellulose biofilm. Cells are stained with mitoTracker
1135 Deep Red (red) and cellulose with Calcofluor-white (cyan). **(E)** 6-nm tomographic slice of a
1136 lamella tomogram of bacterial mat showing three *E. coli 1094* cells and an amorphous cellulose
1137 aggregate between them (orange asterisk). **(F)** 6-nm tomographic slice of a lamella through a
1138 bacterial mat treated with cellulase, showing multiple cells. No cellulose was visible in this
1139 condition. No cortical belt can be seen in the cells in either condition.

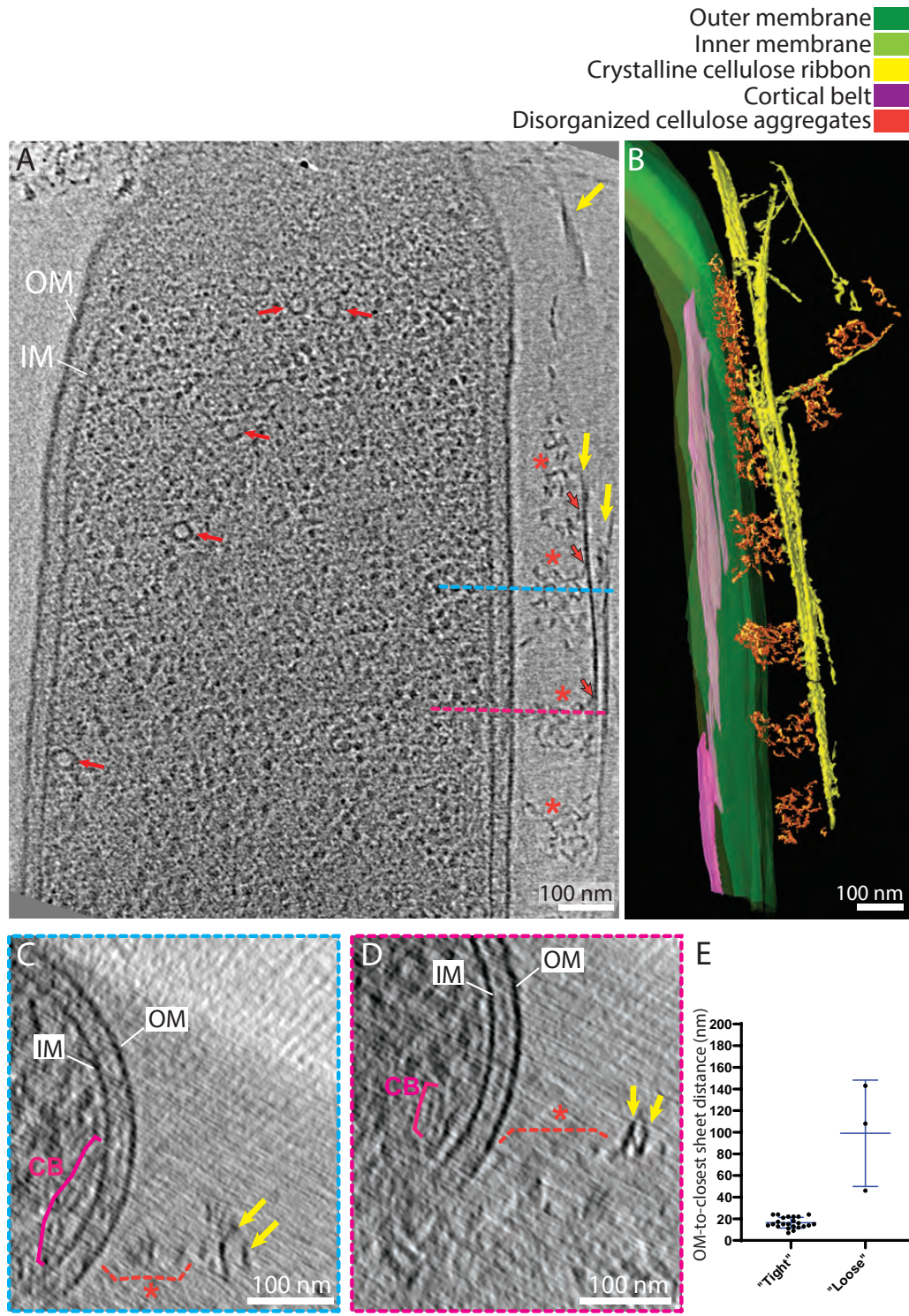
1140

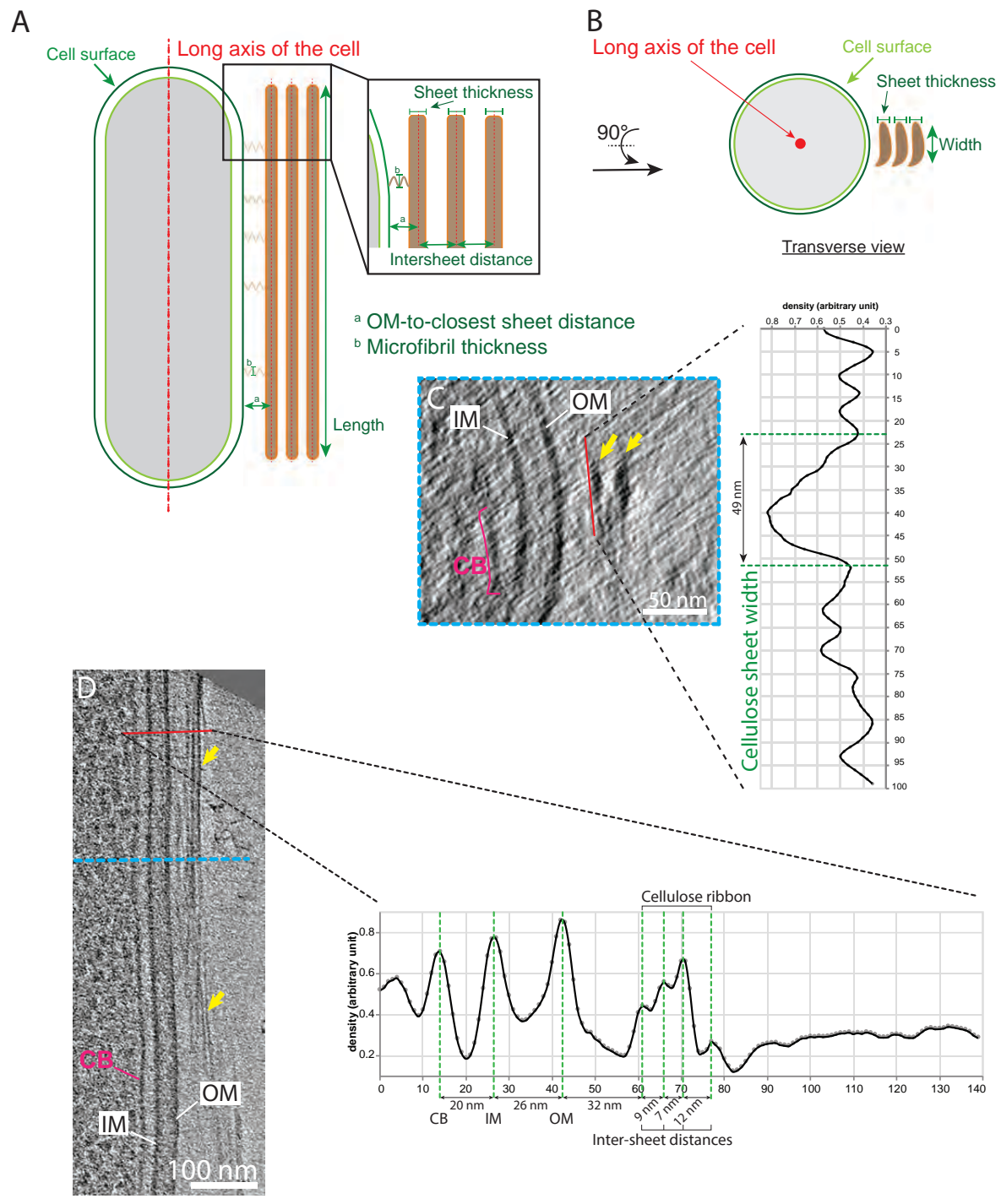
1141 **Figure 9 | Updated cell-directed hierarchical model**

1142 Top (left) and side (right) view of a *G. hansenii* cell showing the different aggregation steps
1143 leading to a cellulose sheet, how microfibrils contribute to sheet width and the role of the

1144 cortical belt. In this model, clusters of 11 extrusion pores are depicted (green circles), the real
1145 numbers and distribution are unknown. Each extrusion pore is presented as comprising 5 BcsC
1146 subunits each (red circles), the actual number is not known. Inset in blue is a magnified view
1147 of the line of 11 extrusion pores, each hypothesized to extrude an aggregate of multiple
1148 elementary fibrils (yellow dashed lines). All aggregates then coalesce to form a microfibril of
1149 increasing thickness as it incorporates an increasing number of elementary fibril aggregates.
1150 These microfibrils then stack together, contributing to the width of the cellulose sheet. Adapted
1151 from the cell in figure 4E-G.







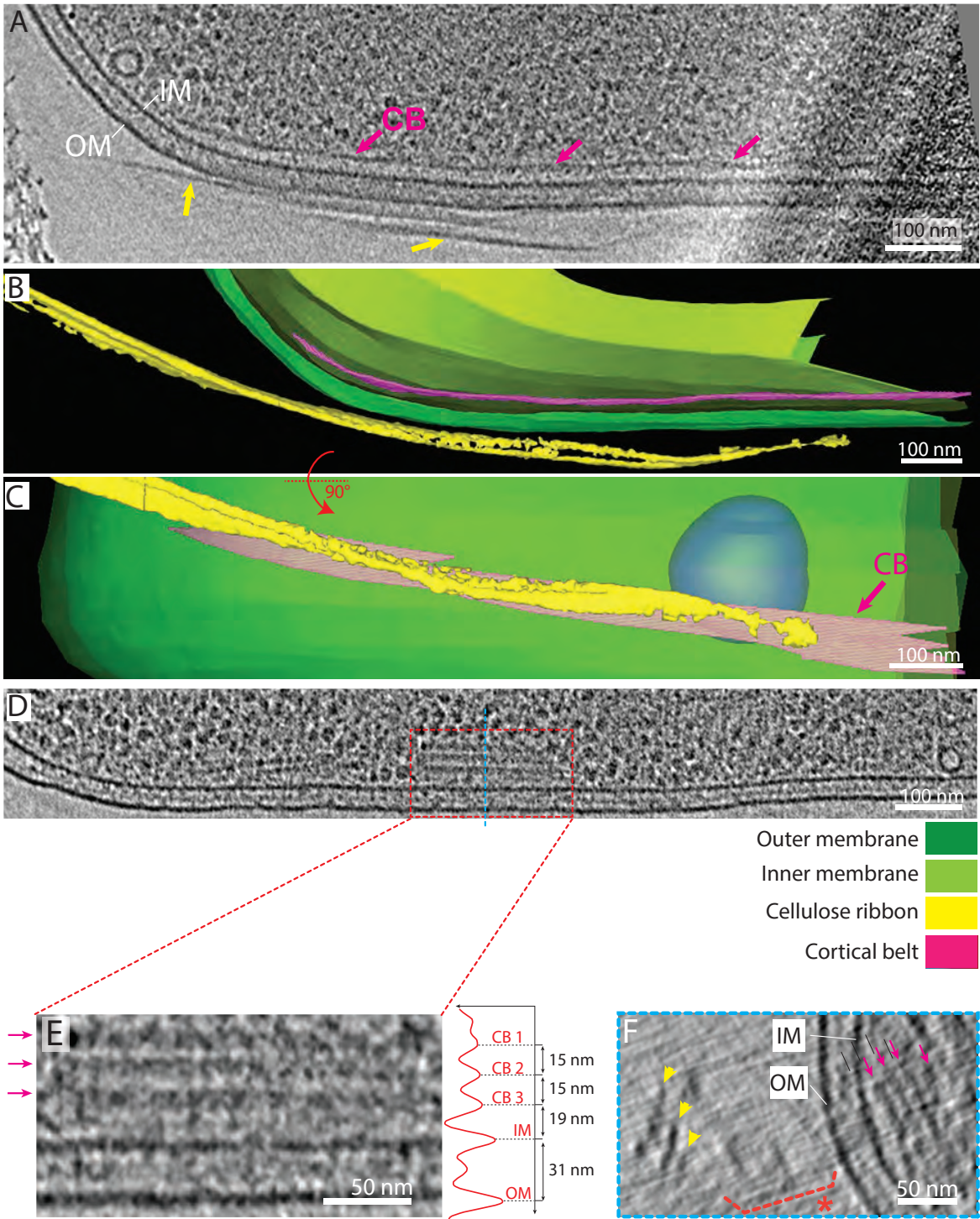
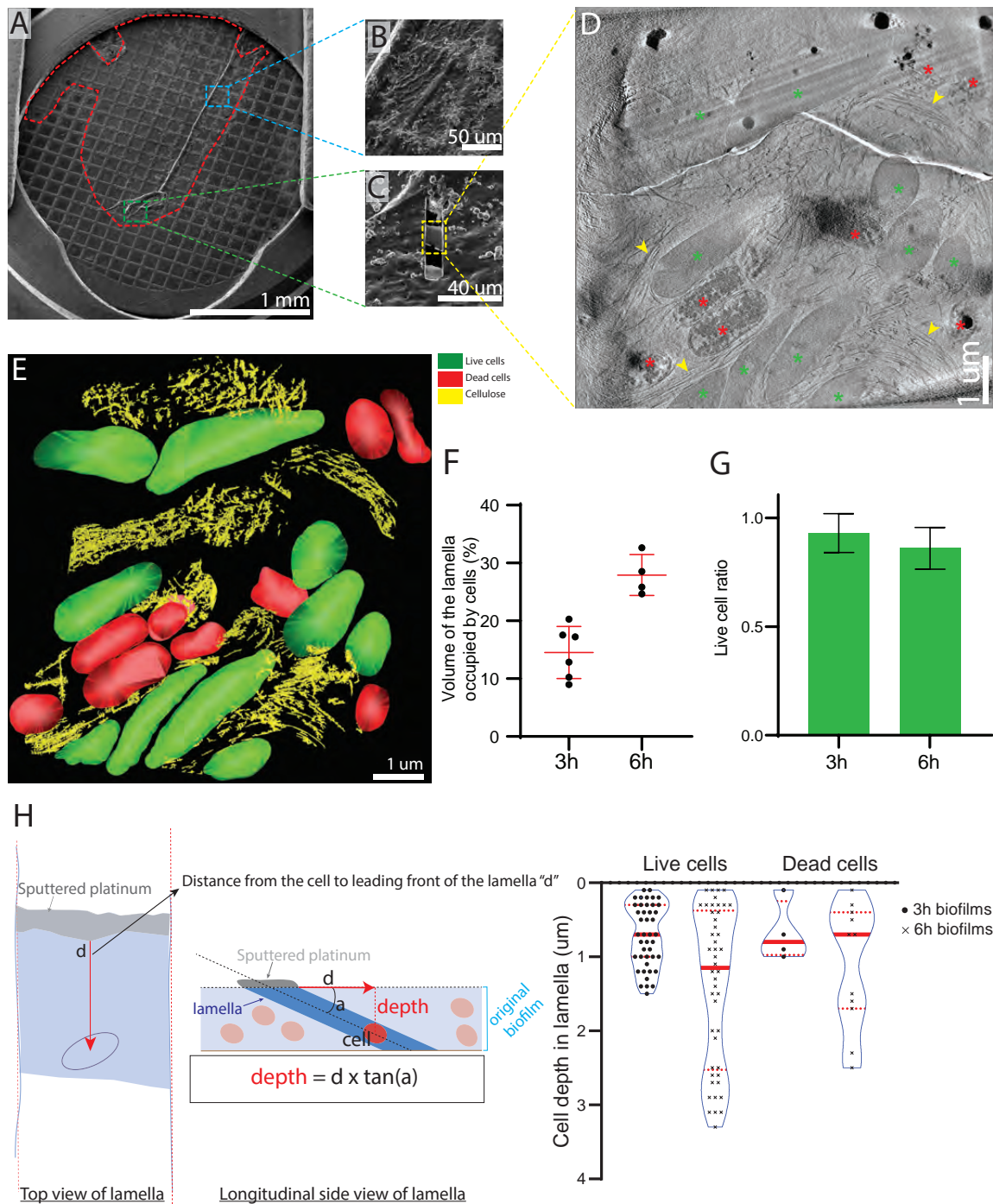
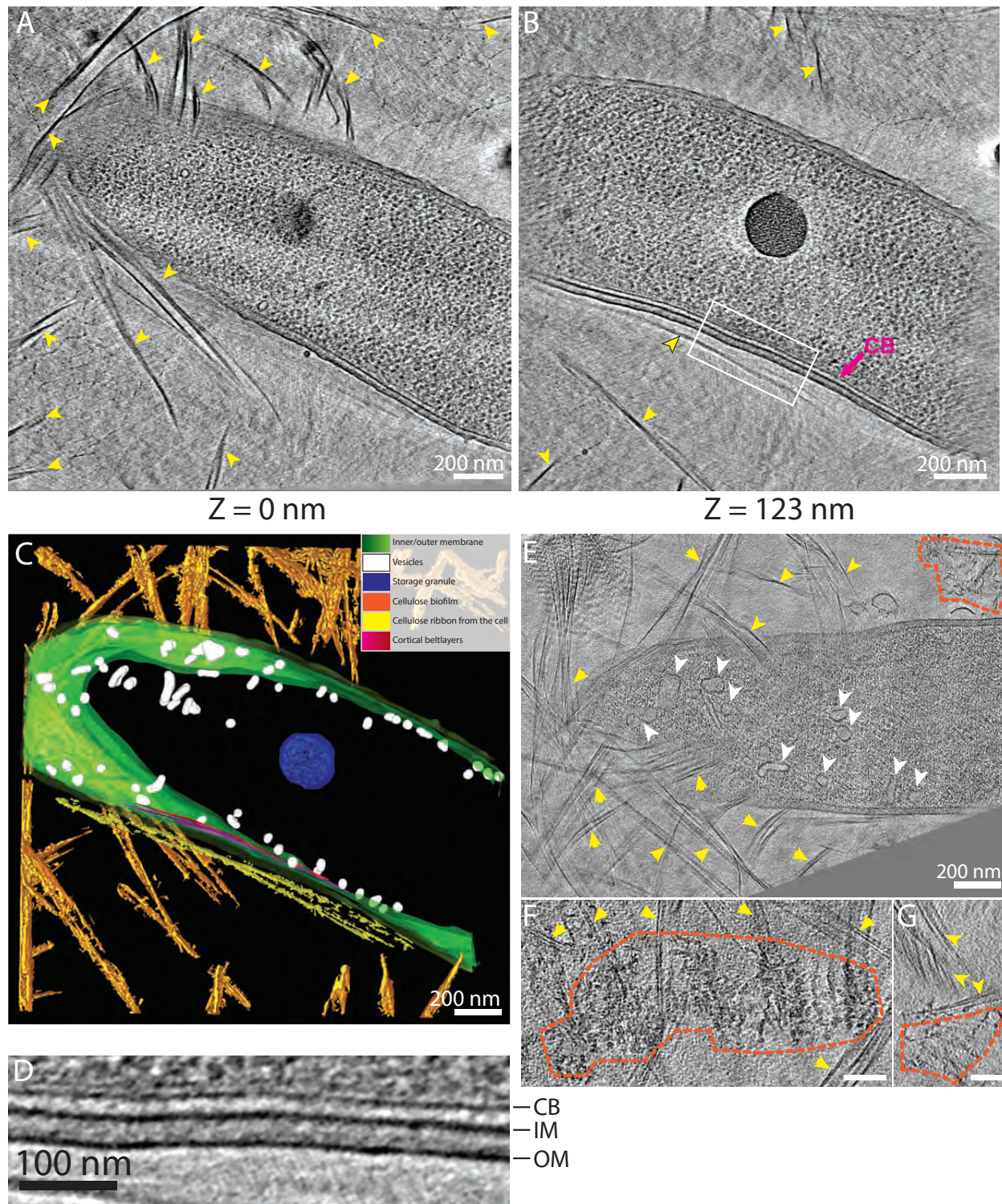
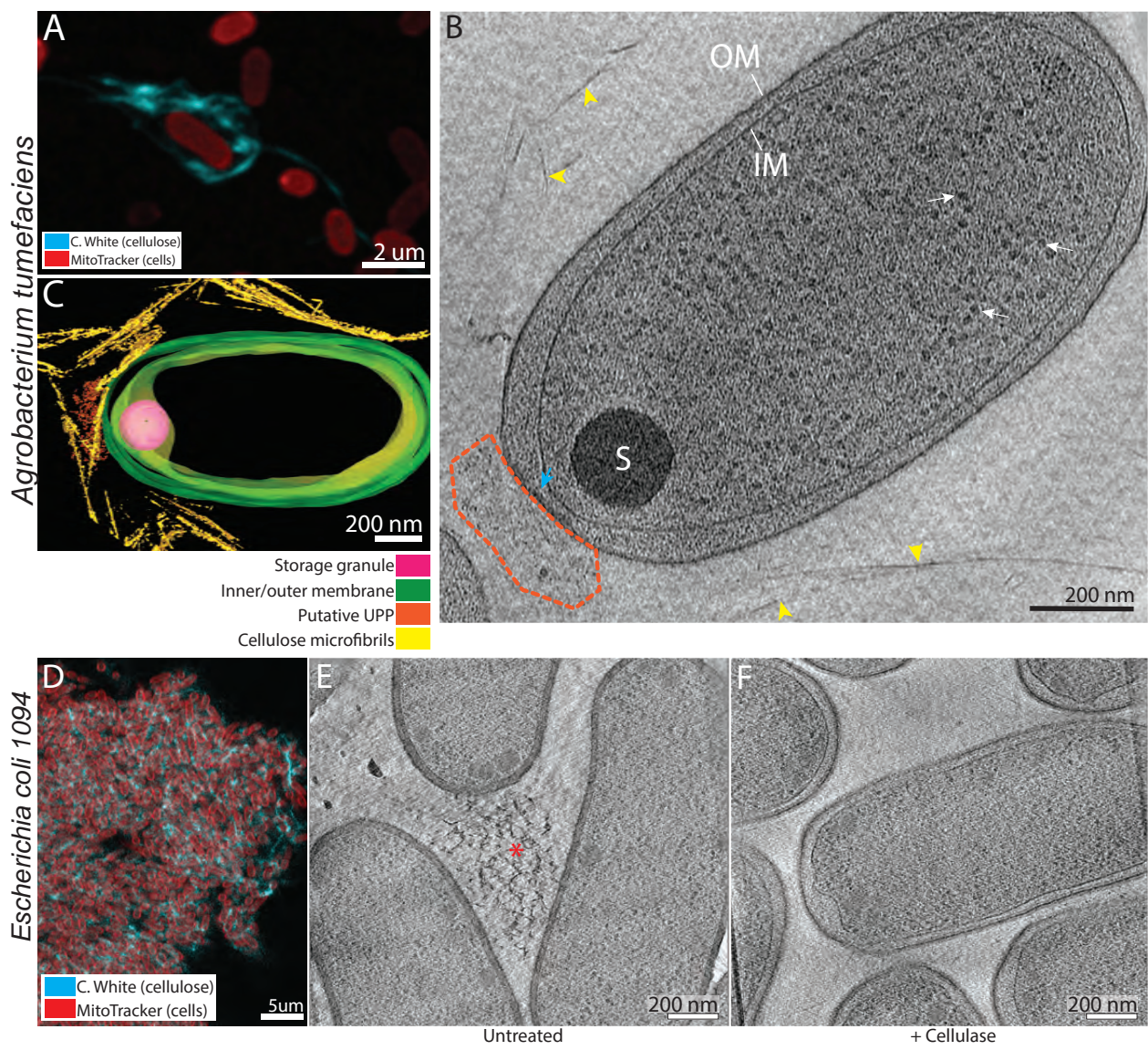


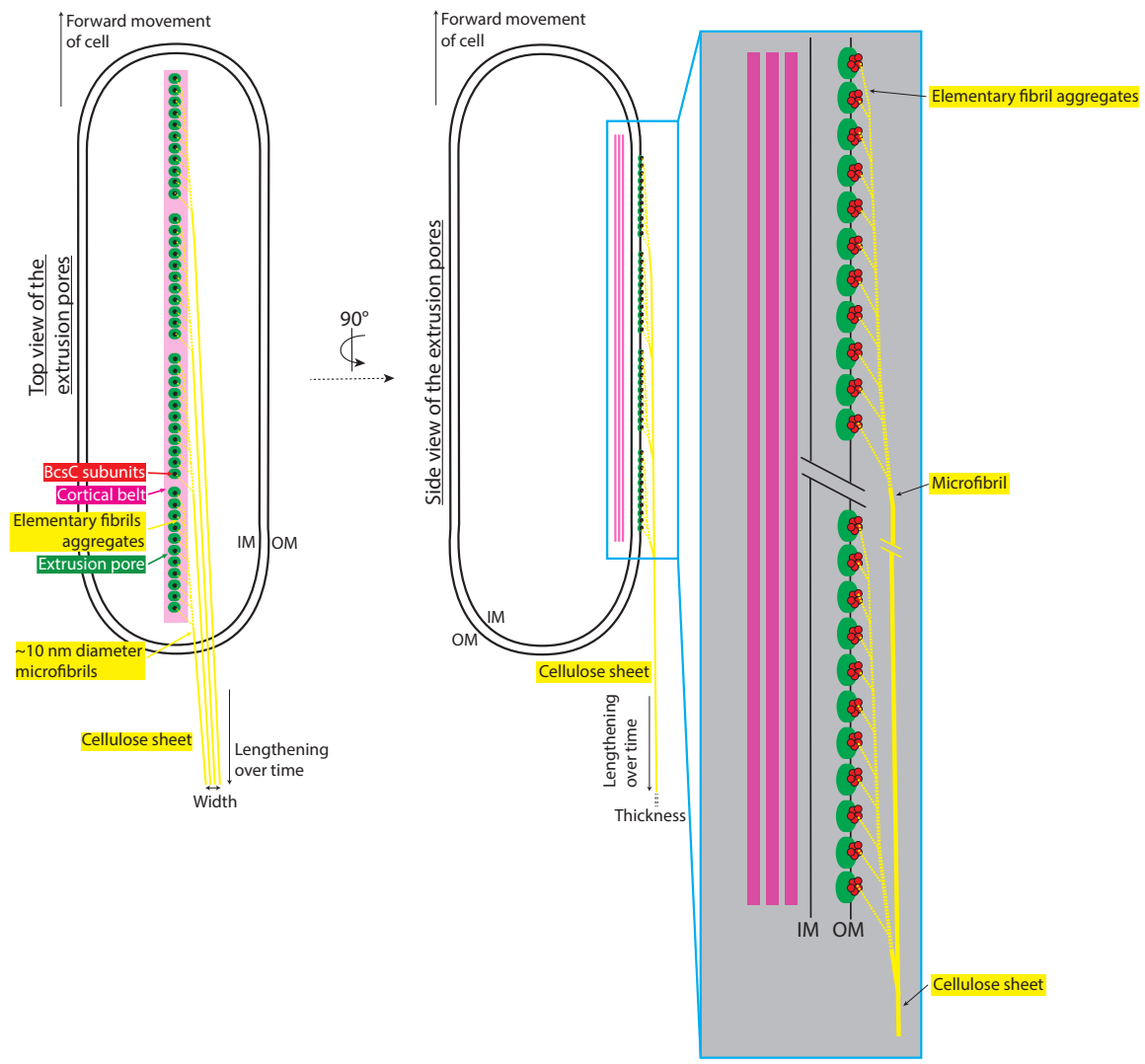
Figure 5 | The cortical belt lies below the cellulose ribbon in the cytoplasm

(A) 9-nm thick tomographic slice showing a representative cortical belt (purple arrows) just inside the IM and proximal to the cellulose ribbon on the outside of the cell (yellow arrows). (B) Manual segmentation of the tomogram shown in (A) highlighting the cellulose ribbon and the cortical belt. (C) Same segmentation rotated 90° about the long axis of the cell shows how the cortical belt and the cellulose ribbon follow the same trajectory. (D) 9-nm thick tomographic slice taken from the same tomogram as in figure 2, showing one out of several cases where the cortical belt presented stacked layers (red dashed box). (E) Enlarged view of the red dashed boxed region in (D) showing the arrangement of the stacked layers. On the right is a density profile displayed normal to the cortical belt to measure the inter-layer distance (15 nm). (F) Transverse 9-nm thick tomographic slice of the cell region shown in (D), at the level indicated by the blue dashed line, highlighting stacked layers of the cortical belt. The cellulose ribbon can be seen at a distance (yellow arrowheads) with disorganized aggregates in between (orange dashed brackets and asterisk).









Whole cell tomography					
Species	Condition/strain	Lamellae	Tomograms	VPP	Source
<i>G. hansenii</i> (ATCC 23769)	Untreated - 13min post sep	N/A	6	-	ATCC
	Untreated - 20min post sep	N/A	14	-	
	Untreated - 300min post sep	N/A	33	24	
	Cellulase 0.2g/L	N/A	4	-	
<i>G. xylinus</i> (ATCC 700178)	Untreated - 5h post sep	N/A	8	-	ATCC
<i>E. coli</i> 1094	Non cellulose induced	N/A	1	-	gift from Jean Marc Ghigo (Institute Pasteur)
<i>Caulobacter crescentus</i>	NA1000 (WT) ³	N/A	1	-	Zhuo Li
<i>A. tumefaciens</i> C58 ^{1,3}	WT ²	N/A	47	-	gift from Patricia Zambrisky (UC Berkeley) to Elitza Tocheva
	A139 ²	N/A	10	-	gift from Patricia Zambrisky (UC Berkeley) to Elitza Tocheva
	AD348 ²	N/A	1	-	gift from Anath Das (University of Minnesota) to Debnath Ghosal
	AD1484 ²	N/A	1	-	gift from Anath Das (University of Minnesota) to Debnath Ghosal
	JX148 ²	N/A	4	-	gift from Patricia Zambrisky (UC Berkeley) to Elitza Tocheva
	NT1 ²	N/A	2	-	gift from Patricia Zambrisky (UC Berkeley) to Elitza Tocheva
Tomography on milled lamellae					
Species	Condition/strain	Lamellae	Tomograms	VPP	Source
<i>G. hansenii</i> (ATCC 23769)	Native biofilm - untreated	12	33	3	ATCC
<i>E. coli</i> 1094 induced for cellulose synthesis	Untreated	2	6	-	gift from Jean Marc Ghigo (Institut Pasteur)
	Cellulase 0.2g/L	1	2	-	

¹ C58 or ATCC 33970 is the wild type *A. tumefaciens*

² All these strains have a C58 background.

³ These strains were imaged for other purposes, but used here as well